

Functional composites by programming entropy-driven nanosheet growth

<https://doi.org/10.1038/s41586-023-06660-x>

Received: 22 February 2023

Accepted: 20 September 2023

Published online: 8 November 2023



Emma Vargo^{1,2}, Le Ma^{1,2}, He Li^{2,3}, Qingteng Zhang⁴, Junpyo Kwon^{2,5}, Katherine M. Evans⁶, Xiaochen Tang⁷, Victoria L. Tovmasyan¹, Jasmine Jan⁸, Ana C. Arias⁸, Hugo Destaillats⁷, Ivan Kuzmenko⁴, Jan Ilavsky⁴, Wei-Ren Chen⁹, William Heller⁹, Robert O. Ritchie^{1,2,5}, Yi Liu^{2,3} & Ting Xu^{1,2,6,10}

Nanomaterials must be systematically designed to be technologically viable^{1–5}. Driven by optimizing intermolecular interactions, current designs are too rigid to plug in new chemical functionalities and cannot mitigate condition differences during integration^{6,7}. Despite extensive optimization of building blocks and treatments, accessing nanostructures with the required feature sizes and chemistries is difficult. Programming their growth across the nano-to-macro hierarchy also remains challenging, if not impossible^{8–13}. To address these limitations, we should shift to entropy-driven assemblies to gain design flexibility, as seen in high-entropy alloys, and program nanomaterial growth to kinetically match target feature sizes to the mobility of the system during processing^{14–17}. Here, following a micro-then-nano growth sequence in ternary composite blends composed of block-copolymer-based supramolecules, small molecules and nanoparticles, we successfully fabricate high-performance barrier materials composed of more than 200 stacked nanosheets (125 nm sheet thickness) with a defect density less than 0.056 μm^{-2} and about 98% efficiency in controlling the defect type. Contrary to common perception, polymer-chain entanglements are advantageous to realize long-range order, accelerate the fabrication process (<30 min) and satisfy specific requirements to advance multilayered film technology^{3,4,18}. This study showcases the feasibility, necessity and unlimited opportunities to transform laboratory nanoscience into nanotechnology through systems engineering of self-assembly.

2D nanosheets, common motifs in natural materials, are readily synthesized and can potentially transform multilayer film technologies^{2,19}. Despite extensive efforts to design layered self-assemblies based on block copolymers (BCPs) and nanoparticles or liquid crystals, a mismatch remains between what is made and what is needed^{6,9,20}. Materials based on easily accessible nanosheets, a few to tens of nanometres in thickness, have generally performed poorly¹⁸. Our inability to translate nanosheets into functional coatings is not unique and reflects deficiencies in current self-assembly approaches. We must holistically engineer nanomaterials to satisfy requirements at the system level, including—but not limited to—feature size, chemistry, multifunctionality, processing, integration compatibility, scalability and life cycle^{3,4,18} (Fig. 1a).

However, every time a new requirement emerges, the design space narrows. Individual nanosheets should be more than 100 nm in thickness to serve as viable components for optical, barrier and dielectric applications^{4,9,21,22}. BCPs with nonlinear chain architectures, such as stars or bottlebrushes, can expand the range of accessible feature sizes and overcome the kinetic barrier associated with long-chain entanglements^{8,9,23–25}. However, their synthesis is demanding. Long-range

order and defect engineering are still out of reach. More critically, the underlying principles defining the phase behaviours are based on specific building blocks under idealized conditions and lack flexibility and adaptability. Nanofillers are essential to expand system chemistries and functions; specific ingredient selections depend on end needs⁶. The conditions used to manufacture integrated nanomaterials at scale will be different from those in the laboratory. The parent BCPs will behave differently in response to variations in substrate surface chemistry, roughness, shape irregularities and the presence of additives, for example, nanofillers^{26,27}. We must improve on current capabilities without laboriously addressing each parameter individually.

The rigidity of existing designs limits programmable nanomaterial growth. Assembling molecules across the atomic-to-macroscopic structural hierarchy is analogous to a multistep chemical reaction with many parallel and sequential steps. The reaction mixture evolves continuously, so we cannot define the identity, concentration, pair interactions and, thus, overall enthalpic contributions of the ‘reactants’. Kinetically, the ‘reactants’ differ in size, shape, diffusivity and diffusion modes. Structure formation leads to geometric confinements and repulsive

¹Department of Materials Science and Engineering, University of California, Berkeley, Berkeley, CA, USA. ²Materials Sciences Division, Lawrence Berkeley National Laboratory, Berkeley, CA, USA. ³The Molecular Foundry, Lawrence Berkeley National Laboratory, Berkeley, CA, USA. ⁴X-ray Science Division, Argonne National Laboratory, Lemont, IL, USA. ⁵Department of Mechanical Engineering, University of California, Berkeley, Berkeley, CA, USA. ⁶Department of Chemistry, University of California, Berkeley, Berkeley, CA, USA. ⁷Energy Technologies Area, Lawrence Berkeley National Laboratory, Berkeley, CA, USA. ⁸Department of Electrical Engineering and Computer Sciences, University of California, Berkeley, Berkeley, CA, USA. ⁹Neutron Scattering Division, Oak Ridge National Laboratory, Oak Ridge, TN, USA. ¹⁰Kavli Energy NanoScience Institute, Berkeley, CA, USA. e-mail: tingxu@berkeley.edu

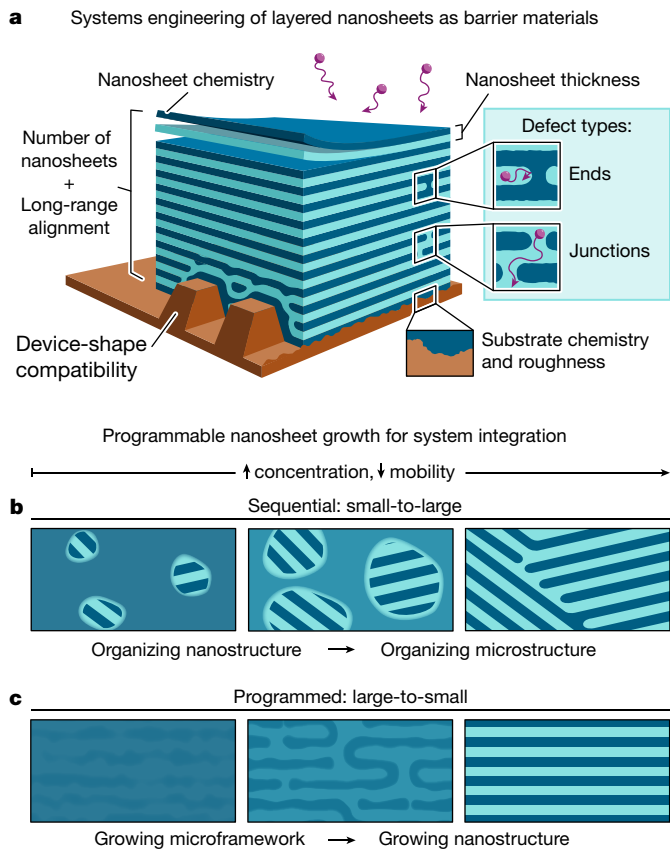


Fig. 1 | Systems engineering of nanosheet barrier materials requires programming the kinetic pathway of nanosheet growth. **a**, To transform stacked nanosheets into high-performance barrier coatings, the assemblies need to satisfy numerous requirements. Sequential growth (**b**) versus programmed nanosheet growth (**c**) during film casting. Sequential growth follows a nano-to-micro-to-macro sequence and forms the smallest feature sizes when the system mobility is the highest. Programmed growth matches the system mobility with the targeted feature size and organizes molecular aggregates into a microframework when the system mobility is high. The nanostructures will subsequently grow within the microframework by means of short-range diffusion when the system mobility is low.

interactions elevate energy barriers for interfacial diffusion^{28–30}. When self-assembly proceeds across a nano-to-micro-to-macro sequence of growth, there is not enough system mobility to organize preformed nanostructures³¹. Although recent progress in machine learning can accelerate design optimization, our knowledge of the kinetics and pathways of nanomaterial growth is too limited to take advantage of these tools^{32,33}.

Here we address these challenges by introducing a new nanomaterial design with two key elements: (1) we use the ability of entropy-driven assemblies to accommodate variations in reactant composition and pair interactions during processing and integration and (2) we match the system mobility with the necessary diffusion of the building blocks to form targeted structures. As shown in Fig. 1b, sequential growth follows a nano-to-micro growth process, in which the smallest structure features form when the system mobility is the highest and vice versa³¹. The proposed growth pathway proposed here proceeds in a reversed, micro-first-nano-later sequence (Fig. 1c): microstructures are defined first when the system has the highest mobility, followed by nanostructure formation through local organization of building blocks¹⁷. Entropy-driven phase behaviour is essential to experimentally realizing this large-to-small growth pathway. It allows the system to form microscopic aggregates in dilute solutions when the system is

mobile enough to organize large-scale structures. Thermodynamically, the entropy-driven phase behaviours seen in high-entropy alloys offer formulation flexibility while maintaining structure fidelity. Thus, target nanostructures can form using many combinations of locally available components when the system mobility is low. Guided by this new design, we successfully fabricate coatings composed of more than 200 stacked nanosheets (125 nm in sheet thickness) with a defect density below $0.056 \mu\text{m}^{-2}$ and approximately 98% efficiency in defect control. The coatings exhibit high-performance barrier properties against volatile organic compounds, water and oxygen for use as packaging, as well as against electrons for use as dielectric capacitors.

System selection

We test the proposed approach using complex blends that exhibit entropy-driven self-assembly. The specific blends are composed of 6-nm zirconium oxide (ZrO_2) nanoparticles, 3-pentadecylphenol (PDP) small molecules and BCP-based supramolecules (abbreviated PS-*b*-P4VP(PDP)) that are constructed by hydrogen-bonding PDP to the pyridine side chains of polystyrene-*block*-poly(vinyl pyridine) (PS-*b*-P4VP)¹³. To the best of our knowledge, these blends are the only known self-assembling system with formulation flexibility and structure fidelity similar to what is observed in high-entropy alloys (Extended Data Fig. 1). They form nanostructures when the effective interactions between PS-rich and P4VP(PDP)-rich microdomains are close to or equal to zero¹⁶. Thus, components can readily diffuse across interfaces, even when the system mobility is low. The P4VP chemistry is beneficial to optimizing the substrate adhesion of the coating.

With an ultimate goal of engineering technologically relevant coating materials, we purposely chose high-molecular-weight BCP-based supramolecules to access the thick nanosheets needed for mechanical robustness and good barrier resistance. The formulations of complex blends, based on BCPs with molecular weights of 134 kDa, 455 kDa and 557 kDa, are listed in Table 1. All components are purchased from commercial suppliers and used as is. They form lamellar or cylindrical microdomains with periodicities ranging from about 60 nm (S1/NP) to about 170 nm (S3/NP). The PDP molecules are dispersed in both the PS-rich and the P4VP(PDP)-rich microdomains; spatially resolved energy-dispersive X-ray spectroscopy (EDS) of S2/NP with iodine-labelled small molecules (I-PDP) is shown in Extended Data Fig. 2. The dispersed PDP molecules screen nonfavourable interactions between PS and P4VP(PDP) and are essential to realize entropy-driven phase behaviours such as formulation flexibility. The proprietary ligand chemistry of the ZrO_2 nanoparticles is unknown, yet S3/NP blends based on 557-kDa PS-*b*-P4VP can accommodate up to 20 vol% of nanoparticles within parallel layers.

The long-polymer-chain entanglements serve several roles: they program the kinetic pathway to match the mobility of the system with its stages of structure evolution and modulate the local defect morphology. The critical overlap concentration of a polymer solution scales as $N^{-1.8}$ in good solvents and is estimated to be >20 vol% for S1 and about 2.7 vol% for S2 based on 134-kDa and 455-kDa BCPs, respectively. By using high-molecular-weight building blocks, the blend forms molecular aggregates in a more dilute solution. This provides sufficient system mobility to organize molecular aggregates into extended microframeworks for subsequent nanostructure formation. The long-chain entanglements increase the kinetic stability and integrity of the aggregates during subsequent growth and organization. Long-chain entanglement can slow down local reorganization at the defect sites and, thus, maintain end-to-end pair-defect morphology.

Nanocomposite formation: kinetic pathway

To program nanosheet growth, we systematically studied S1/NP, S2/NP and S3/NP blends to identify the solution concentrations that

Table 1 | Formulation and compositions of the four blends studied

Blend ID	Supramolecule	PS	P4VP(PDP) ₁	PDP	NP	Morphology
S1/NP	104- <i>b</i> -30(1) kDa	35 vol%	39 vol%	17 vol%	9 vol%	Lamellae
S1 ^{cyl} /NP	104- <i>b</i> -30(1) kDa	35 vol%	39 vol%	23 vol%	3 vol%	Cylinders
S2	330- <i>b</i> -125(1) kDa	32 vol%	47 vol%	21 vol%	0 vol%	Lamellae
S2/NP	330- <i>b</i> -125(1) kDa	29 vol%	43 vol%	19 vol%	9 vol%	Lamellae
S2 ^{dis} /NP	330- <i>b</i> -125(1) kDa	29 vol%	43 vol%	19 vol%	9 vol%	Lamellae
S3/NP	447- <i>b</i> -110(1) kDa	34 vol%	32 vol%	14 vol%	20 vol%	Lamellae

The supramolecule notation includes the molecular weight of the PS and P4VP blocks. PDP molecules are expected to hydrogen-bond to 4VP monomers at a 1:1 ratio, denoted P4VP(1).

form molecular aggregates and lamellar microdomains/nanosheets and quantified the system mobility at nano and micro scales. Using small-angle neutron scattering (SANS) and small-angle X-ray scattering (SAXS), we determined that S2/NP forms molecular aggregates with preferential nanoparticle partitions in the P4VP(PDP)-rich region forming at approximately 10 vol% and well-defined lamellae at a solute concentration of 30 vol%. Figure 2a shows the SANS profiles of S2/NP at solute concentrations of 5 vol% and 10 vol%. Guinier–Porod analysis shows that, at 5 vol%, S2/NP forms fuzzy molecular aggregates, about 100 nm in size and without a preferential partition of nanoparticles³⁴ (details of the model and fits are provided in Extended Data Fig. 3 and Supplementary Information Section 1). At 10 vol%, the molecular aggregates become better defined, with sharper aggregate/solvent interfaces, and nanoparticles preferentially reside in the P4VP(PDP)-rich regions. However, lamellar microdomains have not yet assembled. Ultra-small-angle neutron scattering (USANS) suggests the presence of larger assemblies with an R_g of 453 nm, estimated from a slope transition at $q = 3.8 \times 10^{-3} \text{ nm}^{-1}$ (Fig. 2b). Randomly arranged aggregates were also seen in liquid-cell transmission electron microscopy (TEM) studies (Fig. 2b, inset).

The inhomogeneous distribution of nanoparticles in 10 vol% S2/NP was confirmed using SAXS, which shows a broad correlation hole with a characteristic size of about 114 nm ($q = 0.055 \text{ nm}^{-1}$). This is consistent with its ultra-small-angle X-ray scattering (USAXS) profile in Fig. 2c. The S3/NP blend is based on 557-kDa BCPs and form molecular aggregates at a much lower solute concentration than S2/NP. This is indeed the case: the USAXS profile of S3/NP at a 10 vol% solute concentration shows large-scale assemblies evidenced from strong scattering in the low- q region and emerging nanostructures described by a scattering peak at $q = 0.043 \text{ nm}^{-1}$ (Fig. 2c). In situ SAXS studies showed that well-ordered lamellar microdomains with a periodicity of 126 nm and a Scherrer grain size of about 1.73 μm form almost immediately as the S2/NP solution concentration approaches roughly 30 vol% (Fig. 2d). Aggregates can rapidly transform into nanosheets. Thus, microscopically arranged molecular aggregates can template nanosheet growth and modulate the long-range order of the nanocomposite. For them to do so, however, requires substantial system mobility.

The S2/NP system mobility was quantified using X-ray photon correlation spectroscopy (XPCS) to examine the spatial distribution of the ZrO₂ nanoparticles throughout an in situ drying process³⁵ (Fig. 3e). On the basis of fitting the Kohlrausch exponent γ , nanoparticle diffusion changes from subdiffusive ($\gamma \approx 3.5$) to diffusive ($\gamma \approx 2$) motion as the solute concentration increases from 10 vol% (Extended Data Fig. 4). This is consistent with the SANS results and suggests that nanoparticles leave the meshes of entangled PS to selectively enrich the P4VP(PDP)-rich region. We further quantify the nanoparticle diffusivity at the nano and micro scales by determining the relaxation times at two length scales: τ_s at $q = 0.3 \text{ nm}^{-1}$ and τ_l at $q = 0.03 \text{ nm}^{-1}$ (Fig. 2f). When the molecular aggregates form around 10 vol%, the blend has good mobility for both nanoscopic and microscopic diffusion, with τ_s approximately 100 times faster (10^{-5} s) than τ_l (10^{-3} s). However, when nanosheets form (roughly 30 vol%), the relaxation times increase

sharply ($\tau_l \approx 1,000 \text{ s}$ and $\tau_s \approx 100 \text{ s}$) and are proportional to the diffusion length scales they describe. The system mobility is too limited to alter the templated microstructures. The subsequent nanostructure formation must rely on short-range diffusion to locally organize different building blocks.

We explored the generality of this assembly process using the S1^{cyl}/NP blend, which forms cylindrical microdomains with a periodicity of approximately 80 nm. The drying condition to process S1^{cyl}/NP films was modulated to vary the incubation time (Δt) between the formation of molecular aggregates and the nanostructure formation. *In situ* grazing transmission small-angle X-ray scattering (GTSAXS) was used to characterize the structure evolution throughout the full solution/film thickness over an estimated beam-path length of about 1.5 mm. When the Δt was sufficiently long (about 11 min for this blend), several orders of diffraction peaks appeared rapidly, confirming that mobility-based nanostructure growth can lead to a high degree of long-range ordering in morphologies other than lamellae (Fig. 2g and Extended Data Fig. 5).

Long-range order and defect optimization

The early microscopic structure determines the degree of long-range order of the nanostructure. The step-like changes in the diffusion mode of the nanoparticles and in the system mobilities identify the processing window in which to program micro-first-nano-later growth. The microscopic structure determines the degree of long-range order achieved by the nanostructure. We used rapid solvent removal to kinetically trap the nanocomposite films at specific solute concentrations selected from the scattering results. Representative cross-sectional TEM images of S2/NP films quenched at 23 vol%, 28 vol% and 40 vol% are shown in Fig. 2h (full images are provided in Extended Data Fig. 6). For all samples, nanostructures have clearly formed, despite the rapid solvent removal. This again confirms that nanostructure formation is not the rate-limiting step to hierarchically grow nanosheets. The long-range order is poor when solvent removal occurs at 23 vol%. The solute concentration is too dilute to drive the condensation of molecular aggregates despite high system mobility. With rapid solvent removal at 40 vol%, distinct nanosheets have formed, but the defect density is high and the aspect ratios of the nanosheets are less than 40. This suggests that nanostructure formation can compete with and disrupt microframework formation. The best long-range order is achieved by quenching the film at 28%, slightly below the concentration at which nanosheets have formed. The nanosheets are tens of micrometres in length with aspect ratios greater than 500. Thus, the long-range order, that is, the defect density, can be regulated by optimizing the organization of sheet-like aggregates before nanostructure formation.

Defect type is equally important for barrier performance because different defects have varied effects on transport pathways. The prevalence of different defect types is set by short-range diffusion during the last stages of assembly (full defect densities are provided in Supplementary Information Section 2). Blends based on lower

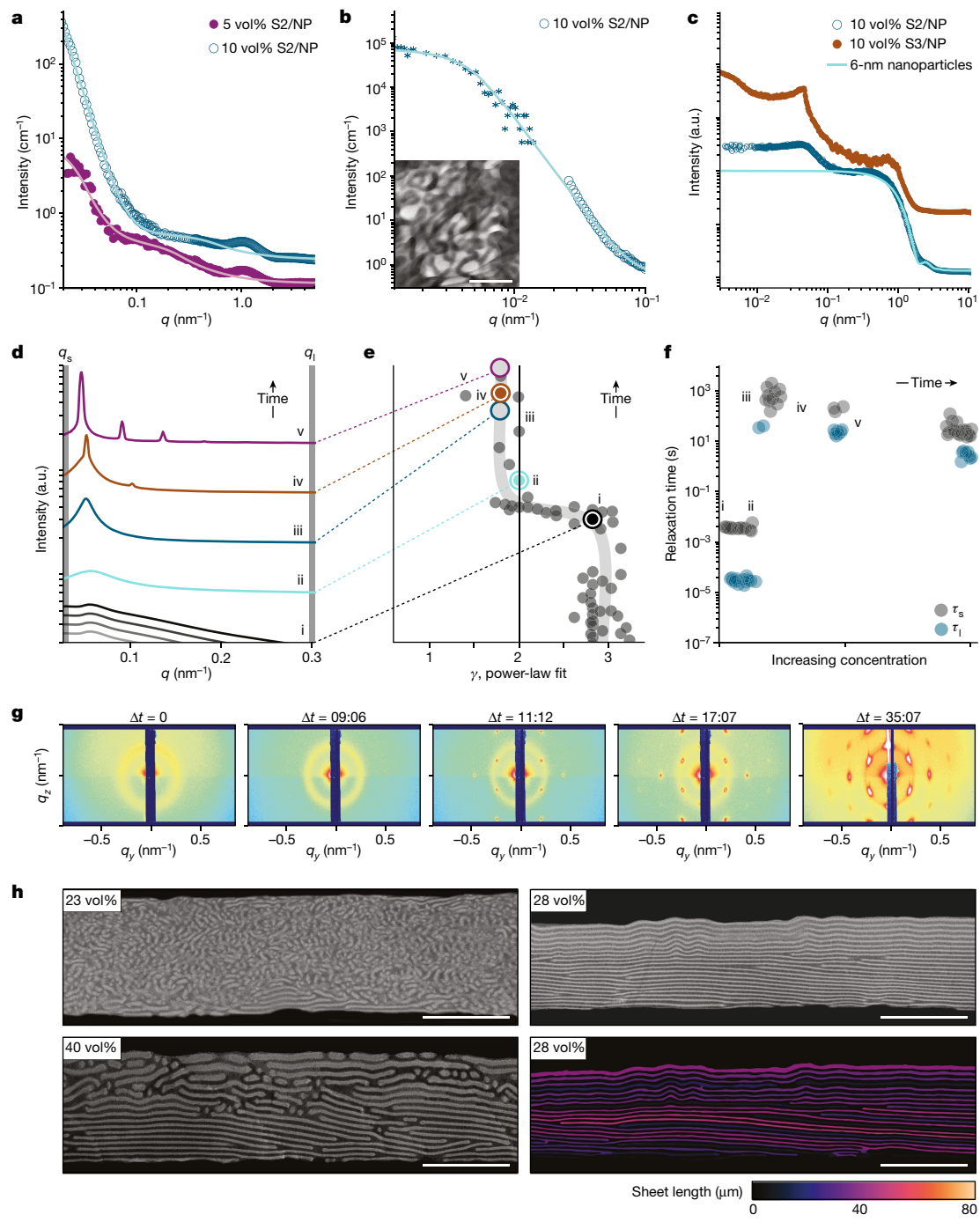


Fig. 2 | Quantification of the nanosheet growth kinetic pathway. **a**, SANS profiles of 5 vol% and 10 vol% S2/NP solutions in deuterated chloroform fitted with Guinier–Porod models. **b**, USANS profile of the 10 vol% S2/NP solution. The inset shows a liquid-cell TEM image of ribbon-like aggregates. Scale bar, 500 nm. **c**, USAXS profiles of 10 vol% S2/NP and S3/NP solutions. At this concentration, the S3/NP solution has formed microscale aggregates, indicated by the presence of low- q features. **d–f**, Results from an in situ SAXS-XPCS experiment used to quantify system mobility during nanosheet growth. Roman numerals i–v refer to the assembly stages during the solvent drying. **d**, SAXS profiles show the structural evolution from a dilute solution to highly ordered lamellae. The q_s and q_l used in panel **f** are labelled. **e**, Nanoparticle diffusion mode evolution during S2/NP assembly process based on Kohlrausch exponent γ . **f**, Comparison of relaxation times τ_s (at $q_s = 0.3 \text{ nm}^{-1}$) and τ_l (at $q_l = 0.03 \text{ nm}^{-1}$) for each assembly stage during nanosheet growth. **g**, In situ GTSAXS of a $S1^{cy}/\text{NP}$ solution under optimized drying conditions. Δt is used to label the elapsed time after aggregate formation (leftmost panel). **h**, Cross-sectional TEM of S2/NP films quenched at labelled solvent fractions. Scale bars, 1 μm . The bottom-right panel is a false-coloured image of the film quenched at 28 vol%, for which colour is used to label the length of each nanosheet extending past the image boundaries. a.u., arbitrary units.

values extracted using kinetics data from q_s to q_l . Each data point is labelled with a filled circle. Note that γ could not be calculated for stages iii and v, owing to the presence of sharp scattering peaks. These stages are labelled chronologically with open circles. **f**, Comparison of relaxation times τ_s (at $q_s = 0.3 \text{ nm}^{-1}$) and τ_l (at $q_l = 0.03 \text{ nm}^{-1}$) for each assembly stage during nanosheet growth. **g**, In situ GTSAXS of a $S1^{cy}/\text{NP}$ solution under optimized drying conditions. Δt is used to label the elapsed time after aggregate formation (leftmost panel). **h**, Cross-sectional TEM of S2/NP films quenched at labelled solvent fractions. Scale bars, 1 μm . The bottom-right panel is a false-coloured image of the film quenched at 28 vol%, for which colour is used to label the length of each nanosheet extending past the image boundaries. a.u., arbitrary units.

molecular weights, for example, S1, have more circular microdomains between nanosheets and sharply bent microdomains, which we have named ‘U-turn’ defects, are uncommon. These defect morphologies

are results of local reorganization and show that the system is mobile enough to reorganize BCP-based supramolecules to release packing frustrations. However, for blends based on high-molecular-weight

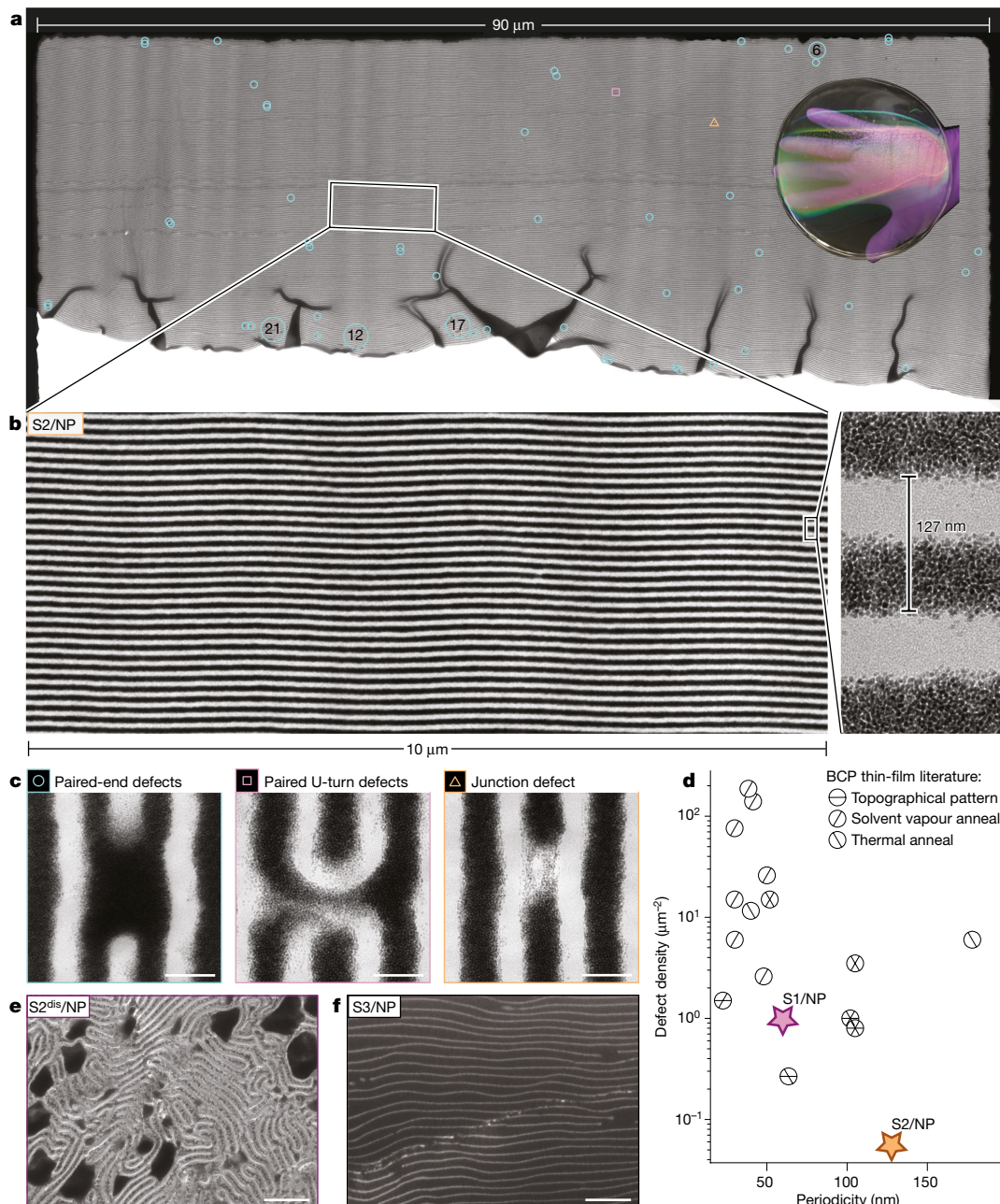


Fig. 3 | Programmed nanosheet growth leads to long-range order and defect control. **a**, Cross-sectional TEM image of an S2/NP coating containing more than 200 stacked nanosheets. Within the approximately $2,660 \mu\text{m}^2$ imaged area, there are only 149 defects: 146 paired ends (blue circles), two paired U-turns (pink square) and one junction (gold triangle). A photograph of an S2/NP coating on a polyester film is shown in the inset. **b**, Higher-magnification TEM images of the S1/NP film showing high-aspect-ratio nanosheets containing

densely packed nanoparticles. **c**, Higher-magnification TEM images of each defect type. **d**, Comparison of defect densities from cross-sectional TEM images of S1/NP and S2/NP with literature values from BCP thin films. **e**, Cross-sectional TEM image of an S2/NP blend dried too quickly for microframework formation; disordered microdomains and nanoparticle aggregates are observed. **f**, Cross-sectional TEM image of an S3/NP film with 20 vol% nanoparticles and a microdomain periodicity of 174 nm. Scale bars, 100 nm.

building blocks, for example, S2/NP and S2, most defects are paired ends and U-turn types. Some nanosheets zigzag into several continuous U-turns (Extended Data Fig. 7 and Supplementary Information Section 3). There is a substantial energy penalty associated with bending the nanosheets at such sharp angles. However, the entanglements of the long chains elevate the energy barrier for local reorganization and kinetically trap these defects after microframework formation³⁶. The U-turn defects can be annihilated by increasing the stiffness of the nanosheets, such as by adding nanoparticles or driving the system to lower solvent fractions, to further enhance the long-range order.

Paired-end defects disconnect the transport pathway and are desirable for engineering barrier materials. Thus, the ability of the long-chain entanglements to decouple defect manipulation from nanostructure formation is advantageous for controlling the prevalence of different defect types³⁶.

Programmed composite coating fabrication

We fabricated macroscopic nanocomposite coatings on commercial membranes by tuning the evaporation of S2/NP solutions to maximize

the time spent between 23 vol% and 28 vol%, with rapid drying afterwards. Figure 3a,b shows a cross-sectional TEM image of a S2/NP film of around 35 μm in thickness. The film includes more than 200 parallel lamellae with a periodicity of 127 nm. Most nanosheets are continuous within and beyond the 90-μm field of view. A similar degree of long-range order extends in other regions of the film (Supplementary Information Section 2). Within the roughly 2,660 μm² imaged area, there are only 149 defects (Fig. 3c and Supplementary Information Section 2). Owing to a lack of reported defect densities for stacked nanosheets, the defect densities of the 60-nm-thick cross-sections were compared with those of BCP thin films (Fig. 3d). The S2/NP defect density of 0.056 μm⁻² is a fraction of densities obtained after multistep annealing treatments (3.5 μm⁻²)³⁷ or topography-directed self-assembly (0.267 μm⁻²)³⁸. We acknowledge that there are obvious system differences, however, and this comparison should not be overinterpreted.

Nearly all the defects are paired ends ($N = 146$ out of 149, about 98%); the remaining defects are paired U-turns ($N = 2$) and a single junction ($N = 1$). Nanoparticles affect the long-range order and defect densities that, in turn, contribute to the properties of the coatings. Nanoparticle incorporation substantially increases the stiffness and bending modulus of the layers. They lead to straight nanosheets with high aspect ratios, low defect density and bias the defect-type distribution away from U-turns and junctions. Kinetic control can more than compensate for the increased entanglement of higher-molecular-weight supramolecules. When the incubation time Δt was reduced, only poorly ordered S1/NP and S2/NP films were observed; sufficiently long Δt led to highly ordered S3/NP films with a periodicity of 174 nm and nanoparticle loading of 20 vol% (Fig. 3e,f).

When engineered at the system level, these nanocomposite films indeed satisfy numerous requirements as functional barrier coatings. With their long-range order and high-molecular-weight building blocks, S2/NP films are flexible and mechanically robust; vibrant structural colour is an added bonus of their relatively large feature sizes. They have an elastic modulus of 512 ± 122 MPa and a hardness of 13.6 ± 3.3 MPa, measured using nanoindentation (Extended Data Fig. 8). Owing to their entropy-driven phase behaviour, stacked nanosheets form on different substrates despite variations in substrate chemistries (silicon, glass, polyester and Teflon) and roughness and shape irregularity³⁹ (Extended Data Fig. 1). Cyclic stretching and buckling tests ($N = 600$) were performed on S2/NP-coated polyester substrates (127 μm thickness, McMaster-Carr) and the coatings retained their integrity with no delamination or crack formation.

High-performance nanocomposite barriers

Essential to product preservation and longevity, barrier materials are a central pillar of sustainability. The multilayered nanocomposite coatings are competitive barrier materials with performance comparable—or superior—to current industry standards and offer notable advantages in their material chemistry and programmable life cycle. Within each nanosheet of a S2/NP film, the nanoparticle-rich region is about 70 nm thick and contains 10–15 layers of densely packed ZrO₂ nanoparticles, reminiscent of a miniaturized metallized film^{21,22} (Fig. 4a). However, these composite coatings have built-in recyclability and provide solutions to recycling issues associated with existing metallized and multilayered films^{21,22}. The long-chain entanglement provides mechanical robustness such that chemical crosslinks are not needed. They are amenable to cycles of assembly, disassembly and reassembly without compromising structure integrity, highlighting the advantages of bottom-up material synthesis (Extended Data Fig. 8).

When coated on porous Teflon membranes, 30-μm S2/NP coatings reduce the permeation of common volatile organic compounds (VOCs) with a removal efficiency of 100 ± 0 % for 2-butanone and

hexaldehyde (kinetic diameter $d_k \geq 5.3$ Å), 96 ± 0 % for acetaldehyde ($d_k = 5.0$ Å), 94 ± 9.2 % for acetone ($d_k = 4.4$ Å) and 55 ± 4.2 % for formaldehyde ($d_k = 3.7$ Å)^{40,41} (Fig. 4e). This performance is comparable with wet scrubbers based on electrochemical cells with a removal efficiency of 95% at a similar VOC concentration⁴². The barrier performance of the composite coating was tested for water-vapour transmission as a substitute for multilayered packaging films. A 30-μm S2/NP coating on a 127-μm polyester film can substantially reduce its water-vapour transmission rate (WVTR) from 11.5 ± 5.7 g m⁻² day⁻¹ to 5.3 ± 0.6 g m⁻² day⁻¹, with more consistent barrier performance over three weeks of testing⁴³ (Fig. 4f and Extended Data Fig. 9).

With 98% efficiency in defect-type control, the nanocomposites with stacked nanosheets are also excellent barriers for electrons, making them high-performance dielectric materials for energy storage^{18,21}. S2/NP films have an energy efficiency of 91.2% at 650 MV m⁻¹ with a charge-discharge efficiency exceeding 90% and a discharged energy density of 6.2 J cm⁻³ (Fig. 4g and Extended Data Fig. 9). This performance is comparable with current industry benchmark dielectrics, including biaxially oriented polypropylene (BOPP) (Fig. 4g and Extended Data Fig. 9). The high dielectric breakdown strength of the nanocomposite film is another testament to the importance of their low defect density and high efficiency in defect-type control.

Organic electronics, including organic light-emitting diodes and photovoltaics, must be encapsulated to prevent degradation by oxygen and water vapour; irregular device topologies present a particular challenge^{44–46}. Calcium films rapidly oxidize under ambient conditions and their relative conductance is a convenient proxy for longer-term device degradation. Electrical calcium tests were used to compare the barrier properties of the S2/NP nanocomposite with two standard ultraviolet (UV)-curable epoxies, DELO Katiobond LP655 and Ossila E132 (Fig. 4h). Despite substantial differences in the barrier thickness, their performances are comparable. A 50% relative conductance of the encapsulated calcium films was reached after 241 ± 27 min for DELO Katiobond LP655 (about 119 μm), 367 ± 53 min for Ossila E132 (about 218 μm) and 79 ± 11 min for S2/NP (about 35 μm). When normalized by the film thickness, the S2/NP barriers nearly double the time until a calcium film reaches 0% relative conductance. Thus, self-assembled nanosheets can lead to thinner and more flexible organic electronics and their built-in recyclability can contribute to better control over the life cycle of organic electronics.

Systematic control studies confirm the importance of holistic nanomaterial design to achieve technologically relevant nanomaterials (Fig. 4e–h). The performance of a barrier material is set by its composition and every aspect of its structure: the layer composition and dimension, defect type and density, long-range order, mechanical properties and geometric conformability. Nanoparticles are instrumental to modulating defect types, achieving entropy-driven phase behaviours and improving barrier, dielectric and mechanical properties. Long-range order of the nanostructure and local defect control are essential to realize the benefits of functional nanomaterials. Poorly ordered S2/NP composites, denoted S2^{dis}/NP, exhibited a greater than 30% reduction in discharged energy density, from 6.2 to 4.3 J cm⁻³, and cannot serve as effective water-barrier coatings. The ordering of nanocomposites also had a pronounced effect on their mechanical properties. Poorly ordered S2^{dis}/NP composites had an elastic modulus of 303 ± 129 MPa, 60% of the ordered value, and a hardness of 1.4 ± 1.4 MPa, only about 10% of the ordered value. Supramolecules formed by high-molecular-weight BCPs are crucial for high performance across every application tested in this study. Contrary to the common belief that chain entanglements are detrimental to assembly kinetics, high-molecular-weight building blocks are advantageous and essential to realize programmable, rapid growth of nanosheets with long-range order and defect control. Excellent barrier performance relies on the thick nanosheets they assemble into. When the nanosheets are only 60 nm in thickness, the barrier efficiency of S1/NP dropped to 20–36% for all VOCs and to <10% for water,

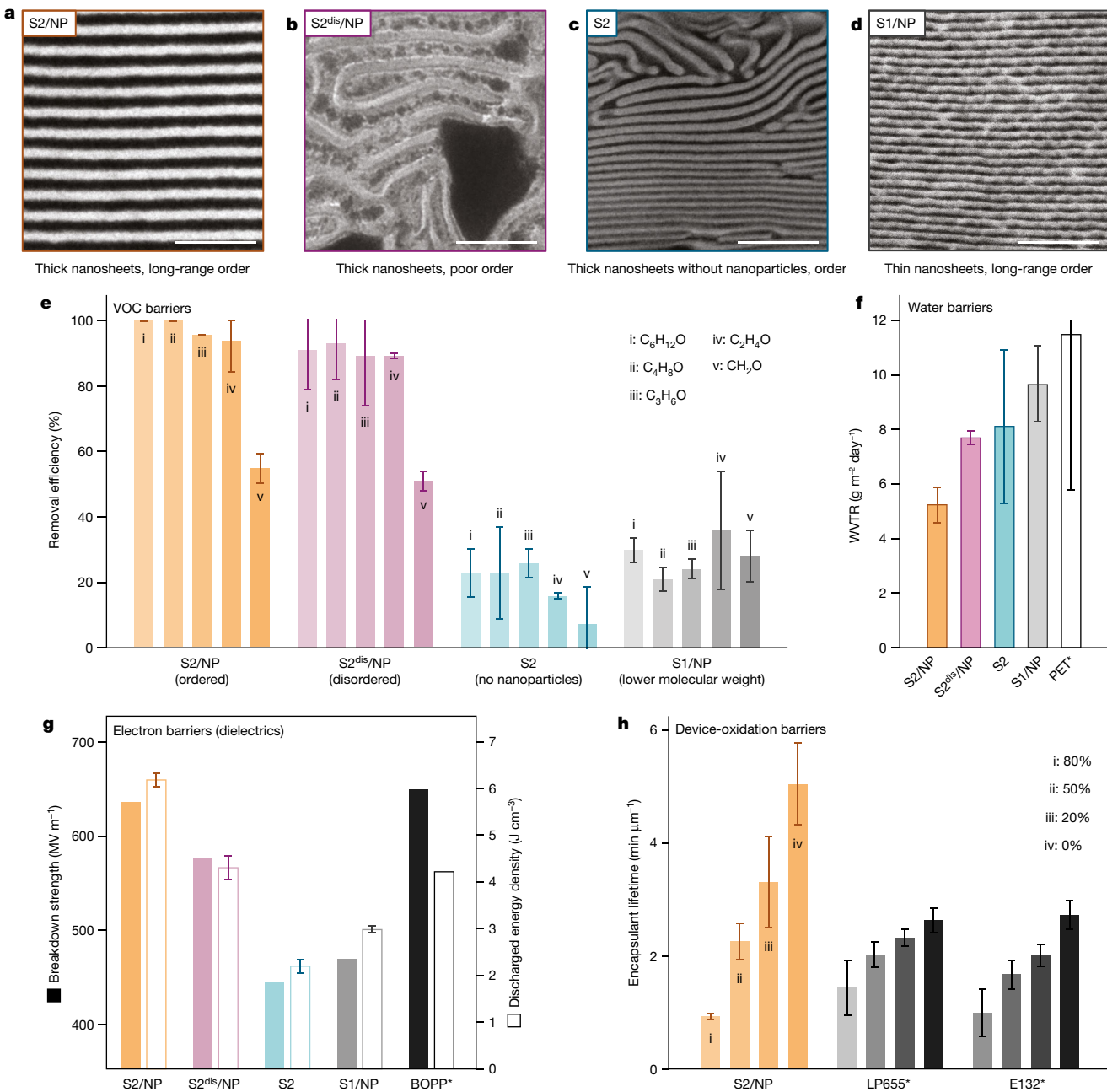


Fig. 4 | Performance evaluation of nanocomposite coatings as barrier materials. **a–d**, Representative TEM images of S2/NP, S2^{dis}/NP, S2 and S1/NP used to establish chemistry–structure–barrier property relationships. Scale bars, 500 nm. **e**, VOC barrier performance for S2/NP, S2^{dis}/NP, S2 and S1/NP coatings on porous Teflon membranes. The removal efficiencies for five VOC molecules are shown. *n* = 2 for each bar. **f**, WVTRs of PET films with S2/NP, S2^{dis}/NP, S2 and S1/NP coatings. S2/NP coatings have the lowest rate of water

transmission. *n* = 3 for each bar. **g**, Dielectric breakdown strength (solid bars) and maximum discharged energy density (open bars) for S2/NP, S2^{dis}/NP, S2 and S1/NP coatings. BOPP is shown as a reference. *n* = 10 for each bar. **h**, Encapsulant lifetimes of S2/NP and two commercial UV-cured epoxies measured using electrical calcium tests. The results are normalized by barrier layer thickness. *n* = 3 for each bar. In all panels, error bars denote ± 1 standard deviation.

and the dielectric breakdown strength dropped from 637 to 469 MV m⁻¹ with a >50% reduction in the maximum discharged energy density.

Conclusion

The successful transformation of nanosheets into high-performance barrier materials highlights the importance and necessity of engineering nanomaterials at the system level. These results confirm the feasibility of converting the trade-offs that limited previous designs into unique advantages, creating nanomaterials that satisfy multifaceted requirements. The present studies demonstrate that

properly engineered nanomaterials are inherently multifunctional and, if designed thoughtfully, will ultimately harness the power of nanoscience to advance technologies. To this end, we must shift from idealized test-tube studies to those under realistic conditions and adopt emerging methods, such as XPCS, to program nanomaterial growth and realize system engineering of nanomaterials.

Online content

Any methods, additional references, Nature Portfolio reporting summaries, source data, extended data, supplementary information,

acknowledgements, peer review information; details of author contributions and competing interests; and statements of data and code availability are available at <https://doi.org/10.1038/s41586-023-06660-x>.

1. Whitesides, G. M. & Boncheva, M. Beyond molecules: self-assembly of mesoscopic and macroscopic components. *Proc. Natl Acad. Sci. USA* **99**, 4769–4774 (2002).
2. Wegst, U. G., Bai, H., Saiz, E., Tomsia, A. P. & Ritchie, R. O. Bioinspired structural materials. *Nat. Mater.* **14**, 23–36 (2015).
3. Bauer, A. S. et al. Recyclability and redesign challenges in multilayer flexible food packaging—a review. *Foods* **10**, 2702 (2021).
4. Alias, A. R., Wan, M. K. & Sarbon, N. M. Emerging materials and technologies of multi-layer film for food packaging application: a review. *Food Control* **136**, 108875 (2022).
5. Lange, J. & Wyser, Y. Recent innovations in barrier technologies for plastic packaging—a review. *Packag. Technol. Sci.* **16**, 149–158 (2003).
6. Balazs, A. C., Emrick, T. & Russell, T. P. Nanoparticle polymer composites: where two small worlds meet. *Science* **314**, 1107–1110 (2006).
7. Lin, Y., Daga, V. K., Anderson, E. R., Gido, S. P. & Watkins, J. J. Nanoparticle-driven assembly of block copolymers: a simple route to ordered hybrid materials. *J. Am. Chem. Soc.* **133**, 6513–6516 (2011).
8. Miyake, G. M., Weitekamp, R. A., Piunova, V. A. & Grubbs, R. H. Synthesis of isocyanate-based brush block copolymers and their rapid self-assembly to infrared-reflecting photonic crystals. *J. Am. Chem. Soc.* **134**, 14249–14254 (2012).
9. Sveinbjörnsson, B. R. et al. Rapid self-assembly of brush block copolymers to photonic crystals. *Proc. Natl Acad. Sci. USA* **109**, 14332–14336 (2012).
10. Santos, P. J., Gabrys, P. A., Zornberg, L. Z., Lee, M. S. & Macfarlane, R. J. Macroscopic materials assembled from nanoparticle superlattices. *Nature* **591**, 586–591 (2021).
11. Qiu, H., Hudson, Z. M., Winnik, M. A. & Manners, I. Multidimensional hierarchical self-assembly of amphiphilic cylindrical block comolecules. *Science* **347**, 1329–1332 (2015).
12. Kao, J. et al. Rapid fabrication of hierarchically structured supramolecular nanocomposite thin films in one minute. *Nat. Commun.* **5**, 4053 (2014).
13. Ikkala, O. & ten Brinke, G. Hierarchical self-assembly in polymeric complexes: towards functional materials. *Chem. Commun.* 2131–2137 (2004).
14. Tsai, M.-H. & Yeh, J.-W. High-entropy alloys: a critical review. *Mater. Res. Lett.* **2**, 107–123 (2014).
15. Frenkel, D. Order through entropy. *Nat. Mater.* **14**, 9–12 (2015).
16. Ma, L. et al. Diversifying composition leads to hierarchical composites with design flexibility and structural fidelity. *ACS Nano* **15**, 14095–14104 (2021).
17. Eliaz, D. et al. Micro and nano-scale compartments guide the structural transition of silk protein monomers into silk fibers. *Nat. Commun.* **13**, 7856 (2022).
18. Baer, E. & Zhu, L. 50th Anniversary Perspective: Dielectric phenomena in polymers and multilayered dielectric films. *Macromolecules* **50**, 2239–2256 (2017).
19. Meyers, M. A., McKittrick, J. & Chen, P.-Y. Structural biological materials: critical mechanics-materials connections. *Science* **339**, 773–779 (2013).
20. Nie, Z., Petukhova, A. & Kumacheva, E. Properties and emerging applications of self-assembled structures made from inorganic nanoparticles. *Nat. Nanotechnol.* **5**, 15–25 (2010).
21. Samant, S. et al. Effect of molecular weight and layer thickness on the dielectric breakdown strength of neat and homopolymer swollen lamellar block copolymer films. *ACS Appl. Polym. Mater.* **2**, 3072–3083 (2020).
22. Kang, Y., Walish, J. J., Gorishny, T. & Thomas, E. L. Broad-wavelength-range chemically tunable block-copolymer photonic gels. *Nat. Mater.* **6**, 957–960 (2007).
23. Gao, H. & Matyjaszewski, K. Synthesis of molecular brushes by “grafting onto” method: combination of ATRP and click reactions. *J. Am. Chem. Soc.* **129**, 6633–6639 (2007).
24. Patel, B. B. et al. Tunable structural color of bottlebrush block copolymers through direct-write 3D printing from solution. *Sci. Adv.* **6**, eaaz7202 (2020).
25. Cummins, C. et al. Strategy for enhancing ultrahigh-molecular-weight block copolymer chain mobility to access large period sizes (>100 nm). *Langmuir* **36**, 13872–13880 (2020).
26. Anastasiadis, S. H., Russell, T. P., Satija, S. K. & Majkrzak, C. F. Neutron reflectivity studies of the surface-induced ordering of diblock copolymer films. *Phys. Rev. Lett.* **62**, 1852–1855 (1989).
27. Tsori, Y., Sivaniah, E., Andelman, D. & Hashimoto, T. Orientational transitions in symmetric diblock copolymers on rough surfaces. *Macromolecules* **38**, 7193–7196 (2005).
28. Dalvi, M. C., Eastman, C. E. & Lodge, T. P. Diffusion in microstructured block copolymers: chain localization and entanglements. *Phys. Rev. Lett.* **71**, 2591–2594 (1993).
29. Dalvi, M. C. & Lodge, T. P. Parallel and perpendicular chain diffusion in a lamellar block copolymer. *Macromolecules* **26**, 859–861 (1993).
30. Huang, J., Qian, Y., Evans, K. & Xu, T. Diffusion-dependent nanoparticle assembly in thin films of supramolecular nanocomposites: effects of particle size and supramolecular morphology. *Macromolecules* **52**, 5801–5810 (2019).
31. Hartgerink, J. D., Beniash, E. & Stupp, S. I. Peptide-amphiphile nanofibers: a versatile scaffold for the preparation of self-assembling materials. *Proc. Natl Acad. Sci. USA* **99**, 5133–5138 (2002).
32. Tu, K.-H. et al. Machine learning predictions of block copolymer self-assembly. *Adv. Mater.* **32**, 2005713 (2020).
33. Vargo, E. et al. Using machine learning to predict and understand complex self-assembly behaviors of a multicomponent nanocomposite. *Adv. Mater.* **34**, e2203168 (2022).
34. Hammouda, B. A new Guinier–Porod model. *J. Appl. Crystallogr.* **43**, 716–719 (2010).
35. Chu, M. et al. pyXPCSviewer: an open-source interactive tool for X-ray photon correlation spectroscopy visualization and analysis. *J. Synchrotron Radiat.* **29**, 1122–1129 (2022).
36. Rubinstein, M. & Colby, R. H. *Polymer Physics* (Oxford Univ. Press, 2003).
37. Choi, E. et al. Substrate-independent lamellar orientation in high-molecular-weight polystyrene-b-poly(methyl methacrylate) films: neutral solvent vapor and thermal annealing effect. *Macromolecules* **47**, 3969–3977 (2014).
38. Park, S. et al. Macroscopic 10-terabit-per-square-inch arrays from block copolymers with lateral order. *Science* **323**, 1030–1033 (2009).
39. Kao, J., Tingsanchali, J. & Xu, T. Effects of interfacial interactions and film thickness on nonequilibrium hierarchical assemblies of block copolymer-based supramolecules in thin films. *Macromolecules* **44**, 4392–4400 (2011).
40. Huang, S.-C., Chung, T.-W. & Wu, H.-T. Effects of molecular properties on adsorption of six-carbon VOCs by activated carbon in a fixed adsorber. *ACS Omega* **6**, 5825–5835 (2021).
41. Li, Y., Li, Y., Feng, X., Chai, Y. & Liu, C. Adsorptive removal of acetaldehyde from propylene oxide produced by the hydrogen peroxide to propylene oxide process. *ACS Omega* **3**, 15272–15280 (2018).
42. Muthuraman, G., Thirumavalavan, M. & Il Shik, M. In situ electrochemically generated peroxymonophosphoric acid as an oxidant for the effective removal of gaseous acetaldehyde. *Chem. Eng. J.* **325**, 449–456 (2017).
43. Seier, M., Archodoulaki, V.-M., Koch, T., Duscher, B. & Gahleitner, M. Polyethylene terephthalate based multilayer food packaging: deterioration effects during mechanical recycling. *Food Packag. Shelf Life* **33**, 100890 (2022).
44. Lu, Q. et al. A review on encapsulation technology from organic light emitting diodes to organic and perovskite solar cells. *Adv. Funct. Mater.* **31**, 2100151 (2021).
45. Castro-Hermosa, S., Top, M., Dagar, J., Fahleitich, J. & Brown, T. M. Quantifying performance of permeation barrier—encapsulation systems for flexible and glass-based electronics and their application to perovskite solar cells. *Adv. Electron. Mater.* **5**, 1800978 (2019).
46. Sutherland, L. J., Weerasinghe, H. C. & Simon, G. P. A review on emerging barrier materials and encapsulation strategies for flexible perovskite and organic photovoltaics. *Adv. Energy Mater.* **11**, 2101383 (2021).

Publisher's note Springer Nature remains neutral with regard to jurisdictional claims in published maps and institutional affiliations.

Springer Nature or its licensor (e.g. a society or other partner) holds exclusive rights to this article under a publishing agreement with the author(s) or other rightsholder(s); author self-archiving of the accepted manuscript version of this article is solely governed by the terms of such publishing agreement and applicable law.

© The Author(s), under exclusive licence to Springer Nature Limited 2023

Methods

Materials

Poly(styrene)-*b*-poly(4-vinyl pyridine) was purchased from Polymer Source, Inc. (polydispersity index = 1.1–1.2). 3-*n*-Pentadecylphenol (90–95% purity) was purchased from Acros Organics. Chloroform was purchased from Fisher Scientific and no HCl was detected using NMR. Deuterated chloroform was purchased from Cambridge Isotope Laboratories. Zirconium dioxide nanoparticles dispersed in toluene (6 ± 2 nm) were purchased from Pixelligent. All materials were used as received, without further purification. In the following methods, the block copolymer is abbreviated PS-*b*-P4VP and the small molecule is abbreviated PDP. The supramolecule is abbreviated PS-*b*-P4VP(PDP) to denote hydrogen bonding between the PDP and 4VP monomers. PDP is added in excess of the possible bonding sites, such that there is more than one PDP molecule for every 4VP monomer. Ratios for each blend are given in Table 1.

Sample solution preparation

PS-*b*-P4VP and PDP powders were dissolved in chloroform to form a 25-mg·ml⁻¹ (2.5 vol%) supramolecule solution. The solution was stirred overnight. For samples that include particles, a separately prepared nanoparticle suspension (25 mg ml⁻¹ ZrO₂ nanoparticles in chloroform) was added to the supramolecule solution and mixed by means of pipette pumping. For the SANS and USANS studies, the same preparation was performed with deuterated chloroform. For the SAXS and XPCS studies, the same preparation was performed with benzene owing to the high X-ray absorption of chloroform. Cross-sectional TEM imaging confirmed that the self-assembly pathway was consistent in benzene and in chloroform.

Drop-cast film sample preparation

For each drop-cast film, a 50-μl droplet of the 2.5-vol% solution was deposited on a 1.5-cm² square-shaped silicon substrate. To slow the drying process, the substrate was sealed within a capped 125-ml glass jar, along with a 70-μl reservoir of pure solvent. The solution was left to dry for a predetermined amount of time (20, 30, 60 or 90 min). At the end of the drying time, the jar was opened and the substrate was quickly removed from the jar. Any remaining solvent evaporated within approximately 3 s, effectively ‘freezing’ the microstructure of the nanocomposite.

A white-light interferometer (Filmetrics F20) was used to measure the thickness of the film as a function of its drying time. At the beginning of the drying process, the thickness of the film is outside the measurement range of the interferometer. These thickness values were estimated by interpolating between the known initial film thickness (calculated from the solvent volume and substrate area) and an exponential decay fit of the later drying data. Thickness values were converted into solvent or solute fractions to compare results across different experiments.

Bulk sample preparation

To prepare the bulk samples, 1 ml of the 2.5-vol% polymer solution was dried in a 1-ml Teflon beaker at room temperature. The beaker was not sealed or covered, so solvent was allowed to evaporate freely. Because of the larger volume of solvent, the sample was left to dry overnight. Once dried, the nanocomposite was peeled from the Teflon beaker using tweezers. To prepare intentionally disordered samples, a jet of N₂ was directed across the opening of the beaker. This sped the drying process to about 30 min.

Static solution SANS and USANS experiments

The EQ-SANS instrument of the Spallation Neutron Source of Oak Ridge National Laboratory was used for the SANS experiments⁴⁷. The temperatures of the samples, which were contained in cylindrical quartz cuvettes, were maintained at $25 \pm 0.1^\circ\text{C}$. Each sample was

measured using three settings of the sample-to-detector distance and minimum wavelength: 9 m/15 Å, 4 m/10 Å and 2.5 m/2.5 Å. Collectively, these three configurations span a range of momentum transfers, q , of $0.002 \text{ \AA}^{-1} < q < 0.7 \text{ \AA}^{-1}$. The data from the samples and the solvent were corrected for wavelength-dependent transmission, incident flux, detector sensitivity, geometric effects and the signal from the empty quartz cell before being azimuthally averaged and binned into $1\text{D}/(q)$ versus q using the standard procedures implemented in the drtsans software⁴⁸. During data reduction, the data were scaled into absolute intensities of 1 cm⁻¹ using a calibrated porous silica standard⁴⁹. Then, the data from the three instrument configurations were merged into a single dataset. The merged datasets were used for the data analysis.

USANS measurement was conducted on the BL-1A USANS instrument at the Spallation Neutron Source collectively using three wavelengths of 1.2, 1.8 and 3.6 Å to cover the wavevector q range from 5×10^{-5} to $3 \times 10^{-3} \text{ \AA}^{-1}$. The samples were loaded into 2-mm Hellma cells. The data were reduced with empty-cell background correction and presented in absolute intensity units.

Guinier–Porod fits were performed in Igor using the Irena package developed at the Advanced Photon Source⁵⁰. Details of the Guinier–Porod fits and interpretation are provided in Extended Data Fig. 3 and as Supplementary Information Section 1.

Static solution SAXS

Absolutely calibrated USAXS and SAXS experiments were performed at beamline 9-ID at the Advanced Photon Source, Argonne National Laboratory¹². The combined q range is between $1 \times 10^{-4} \text{ \AA}^{-1}$ and 1.3 \AA^{-1} ; here $q = 4\pi/\lambda \sin(\theta)$, in which λ is the wavelength and θ is half of the scattering angle. The X-ray energy was 21 keV ($\lambda = 0.5895 \text{ \AA}$). X-ray photon flux was approximately equal to $5 \times 10^{12} \text{ mm}^{-2} \text{ s}^{-1}$ through a beam size of $0.5 \times 0.5 \text{ mm}$. Data were reduced using USAXS instrument data reduction software and were desmeared from slit-smeared collimation of the Bonse–Hart USAXS system.

In situ SA-XPCS

In situ small-angle X-ray scattering and X-ray photon correlation spectroscopy (SA-XPCS) experiments were performed at beamline 8-ID-I at the Advanced Photon Source, Argonne National Laboratory. The X-ray energy is 10.9 keV; the horizontal beam size is 15 μm, as defined by the upstream guard slits, and the vertical beam size is 10 μm. To perform the drying experiments, 10-vol% S1/NP solutions were loaded into quartz capillaries (2 mm outer diameter, Charles Supper). The capillaries were unsealed so that the solvent could freely evaporate. Owing to the small surface area of the capillary, the drying process took approximately 12 h. Scattering data were collected every 15 min. The diffusion of the liquid within 15 min was sufficient to avoid visible beam damage. Other than the known starting concentration, the local solution concentration could not be measured during the drying process. The 2D scattering intensity was collected using a Rigaku XSPA-500k detector. The fast dynamics (early stages of drying) were captured at a 50-kHz frame rate with a total acquisition time up to 2 s. The slow dynamics (later stages of drying) were captured at a 100-Hz frame rate with an adjustable total acquisition matching the timescales of the sample (50 s in this study). The SA-XPCS analysis was performed on high-performance Clusters using the APS Data Management System workflow⁵¹. Both the SAXS and XPCS results were visualized, fitted and plotted using the graphic modules and the function libraries provided by pyXPCsviewer³⁵. Examples of the raw XPCS data and τ fits are provided in Extended Data Fig. 4.

GTSAXS

GTSAXS measurements were performed at beamline 8-ID-E at the Advanced Photon Source, Argonne National Laboratory. The X-ray wavelength was 1.687 Å and the scattering intensity distribution was captured by a Pilatus 1M detector. A 2 × 2-cm silicon substrate was placed in a chamber designed for in situ measurements and aligned

with the beam. A chloroform reservoir of a selected volume (here 350 or 500 µl) was injected into the chamber to slow the drying process and then 100 µl of sample solution was drop-cast onto the substrate. GTSAXS measurements were taken at an incident angle of 0.8°.

TEM sample preparation and imaging

Bulk samples were embedded in resin (Araldite 502, Electron Microscopy Sciences) and cured at 60 °C overnight. Film samples were coated with resin and cured at 60 °C overnight. The silicon substrates were removed by submerging the resin-coated films in liquid nitrogen; owing to mismatched thermal expansivities, the nanocomposite film peeled away from the silicon and remained attached to the resin. Sections about 60 nm in thickness were microtomed using an RMC MT-X ultramicrotome (Boeckeler Instruments), floated on top of water and picked up on copper TEM grids. For samples without nanoparticles, iodine vapour was used to selectively stain the P4VP region. The thin sections were imaged using a FEI Tecnai 12 at an accelerating voltage of 120 kV. To produce high-resolution composite images (Fig. 3a and Extended Data Fig. 6), overlapping TEM images were collected and manually aligned in Photoshop using lower-magnification reference images.

Automatic nanosheet length and defect analysis

Image analysis code was performed in Python, using approaches translated from ADABlock, an ImageJ plugin developed by Murphy et al.⁵² In brief, greyscale TEM images were binarized using a local Otsu thresholding technique. The binarized images were used to draw 1-pixel-thick skeletons that described the connectivity of the cross-section of each layer. The eight nearest neighbours of each skeleton pixel were used to label defects. A skeleton pixel with two nearest neighbours was considered defect-free, a skeleton pixel with only one nearest neighbour was labelled an end and a skeleton pixel with three or more nearest neighbours was labelled a junction. Connected junctions were combined to avoid double-counting. Because U-turn defects do not affect connectivity, they were not counted in this automated image-analysis routine. Each end defect was examined manually and U-turn defects were labelled as applicable.

To perform the sheet-length analysis, all junction pixels were deleted from the skeleton, leaving a set of isolated 1D sheets. The length of each sheet was tallied in pixels and then converted to micrometres using the magnification of each image.

VOC removal efficiency tests

Films of S2/NP, S2^{dis}/NP, S2 and S1/NP were prepared on circular 47-mm-diameter polytetrafluoroethylene air-sampling membranes (Pall, part number R2PJ047). In each test, the rim of the specimen was tightly held between the two flanges of a Teflon filter holder, which were fitted with 1/4" Teflon tubing. On one side, the filter holder was connected to a Teflon bag pre-filled with air that was enriched with a mixture of formaldehyde (70–230 ppb), acetaldehyde (10–90 ppb), acetone (1.9–4.3 ppm), 2-butanone (35–90 ppb) and hexaldehyde (40–95 ppb). Water vapour was added to the bag to achieve a relative humidity of 5–50%. Experiments were performed at room temperature (20–23 °C). Temperature and relative humidity were measured with an in-line digital T/RH sensor (HIH6100 series, Honeywell). On the other side of the filter holder, air was drawn from the bag through the specimen using a peristaltic pump that operated at a flow of 80–90 ml min⁻¹. Once air flow through the specimen reached a steady-state regime, samples were collected simultaneously upstream and downstream of the specimen, by pulling air through 2,4-dinitrophenylhydrazine (DNPH)-impregnated silica gel cartridges (Waters Corp., part number WAT047205), over periods of 15–50 min.

DNPH cartridges were subsequently extracted with 2 ml of carbonyl-free acetonitrile (Honeywell) and the extracts were analysed by high-performance liquid chromatography with UV detection (Agilent 1200), following the TO-11 method of the United States Environmental

Protection Agency⁵³. The VOCs were identified on the basis of the retention times of authentic standards corresponding to their dinitrophenylhydrazine derivatives (Sigma-Aldrich). These standards were used to develop calibration curves for quantification. Reported values are the average of duplicate determinations obtained sequentially. The retention efficiency E_i of each compound i was determined as

$$E_i = \frac{C_i^{\text{up}} - C_i^{\text{down}}}{C_i^{\text{up}}} \times 100$$

in which C_i^{up} and C_i^{down} are the simultaneously measured upstream and downstream concentrations of compound i , respectively.

WVTR tests

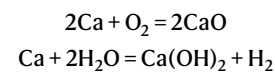
The WVTR test set-up was informed by ASTM E96-00: 'Standard Test Methods for Water Vapor Transmission of Materials'⁵⁴. For each test, an aluminium jar (80 mm diameter, Joywee) was filled with 4 g of desiccant pellets (DampRid Moisture Absorber). A polyester sheet (127 µm thickness, McMaster-Carr) was heat-sealed around the mouth of the jar, forming a circular dish with a 5-mm rim. Once cooled, the circular dish was removed from the jar and filled with 2.5 ml of 2.5-vol% sample solution. After the film dried, the polyester dish was turned upside down and glued with 5 Minute Epoxy (Devcon) to the desiccant-filled jar, creating a seal. Control samples were prepared following the same procedure, with 2.5 ml of pure chloroform substituted for the sample solution.

The initial weight of the sample was taken directly after the commercial epoxy bonded the sample to the dish cured. Samples were then placed on a perforated plastic platform above salt-saturated water, all within a sealed plastic container at ambient temperature and pressure to generate a 75% relative humidity environment⁵⁵. Weight measurements were taken once every 24–48 h to measure desiccant water mass gain through the test film, for three weeks after the initial weight was measured. The WVTR values were calculated by finding the least-squares fit of the sample mass versus collection time data. The slope of the fit was converted into a WVTR by dividing by the film area, $A = 40\pi \text{ mm}^2$, for the jars used here. The standard deviation of the WVTR was calculated in the same way.

$$\text{WVTR}(\text{g m}^{-2} \text{ day}^{-1}) = \frac{m_f - m_i}{A(t_f - t_i)}$$

Calcium conductivity tests

Electrical calcium tests were used to compare the barrier properties of the nanocomposite with commercially available UV-curable epoxies. Each sample was prepared on a 125-µm polyethylene terephthalate (PET) substrate through a series of thermal-evaporation steps. A pair of silver traces (100 nm thick, 2 × 15 mm² in size, 4 mm spacing) was thermally evaporated on the PET substrate. Calcium (100 nm thickness, 8 × 8 mm² in area) was thermally evaporated (pressure of 2–5 × 10⁻⁶ Torr, deposition rate <0.8 Å s⁻¹) on top of the silver, electrically connecting the two traces and resulting in an initial conductance of <0.1 S. Each sample was then prepared with the designated encapsulant and covered with a 125-µm PET cap. The decreasing conductance of the calcium sample is a result of oxidation in the presence of oxygen and moisture:



The commercial epoxies tested were DELO Katiobond LP655 and Ossila E132 epoxy. After application of the epoxy and PET cap, each sample was exposed to a UV lamp until fully cured before measurement. For nanocomposite samples, about 20 µl of S2/NP solution was

Article

drop-casted, covered with the PET cap and left to assemble for about 1 h before measurement. Conductance of the encapsulated samples were measured over time (Keysight DAQ970A) in an enclosed environmental chamber (Associated Environmental Systems BHS-503, Acton) maintained at 20% relative humidity and 20 °C. The approximate barrier thickness for the commercial encapsulants were calculated on the basis of the repeated weight measurements of applied drops and the volumetric densities reported by the manufacturers.

Dielectric tests

Device fabrication. Indium tin oxide (ITO)-coated glass substrates ($2\text{--}3 \Omega \text{ sq}^{-1}$, Thin Film Devices, Inc.) were pre-cleaned using soapy water, deionized (DI) water, acetone and isopropanol, sequentially. The substrates were then heated at 100 °C for at least 4 h, followed by UV/O₃ treatment for 20 min before use. Nanocomposite films were drop-cast on the ITO substrates as described above. After the films dried fully, they were placed in a vacuum chamber overnight to remove any residual solvent or moisture. The typical film thickness was about 2 μm.

Gold electrodes (1.13 mm² area with approximately 20 nm thickness) were deposited on the top surface of the film samples using a thermal evaporator (MBRAUN). The ITO conductive coating was electrically connected to the ground using conductive silver paint (Ted Pella, Inc.). For comparison, benchmark BOPP (capacitor grade, about 3–4 μm) was obtained from PolyK Technologies, LLC. Gold electrodes (1.13 mm² area with approximately 20 nm thickness) were deposited on both sides of the BOPP films using the same thermal evaporator (MBRAUN).

Device breakdown strength. Dielectric breakdown strengths were measured using a Trek 610D instrument amplifier as the voltage source based on an electrostatic pull-down method, in which a DC voltage ramp of 200 V s⁻¹ was applied to the film samples until dielectric failure. The experimental dielectric breakdown measurements were analysed with a two-parameter Weibull statistic, which can be described as

$$P(E) = 1 - \exp(-E/\alpha)^{\beta},$$

in which $P(E)$ is the cumulative probability of dielectric failure, E is the measured dielectric breakdown field, the scale parameter α is the characteristic breakdown strength (that is, Weibull breakdown strength), which corresponds to a failure probability of 63.2% and the shape parameter β is associated with the distribution of data. A higher β value refers to a narrower data spread. At least ten measurements were performed for each Weibull fitting.

Dielectric energy storage properties. Electric displacement–electric field (D – E) loops were collected under varied applied electric fields using a modified Sawyer–Tower circuit, which is integrated with a PK-CPE1801 high-voltage test system from PolyK Technologies, LLC. The voltages with a unipolar triangular waveform were applied to the film samples at a frequency of 100 Hz. Dielectric energy storage properties including discharged energy density and charge–discharge efficiency were derived from D – E loops.

Mechanical tests

Nanoindentation. Nanoindentation was performed to measure the reduced modulus and hardness of the nanocomposite coatings. We used a Hysitron TI-950 Triboindenter with a Berkovich tip (TI-0039-1, 50 nm tip radius). The coatings were attached to a silicon wafer using crystal bonds and placed at ambient conditions overnight for indentation. Twenty-five indentations were performed per sample with a maximum load of 1,000 μN and a loading rate of 20 μN s⁻¹. The films were subjected to quasistatic indentation with a hold time of 30 s before unloading. The applied tip-area function was fitted using the reference material, polycarbonate, provided by Hysitron.

The Oliver and Pharr method was used to determine the reduced modulus and hardness⁵⁶. The reduced modulus is defined as

$$\frac{1}{E_r} = (1 - \nu^2 E)_{\text{sample}} + (1 - \nu^2 E)_{\text{indenter}},$$

in which the modulus of elasticity, E_{indenter} , is 1,140 GPa, and the Poisson's ratio of the indenter, ν_{indenter} , is 0.07. The Poisson's ratio of the sample was assumed as 0.34 to convert from the measured reduced modulus to the elastic modulus.

Cyclic buckling test. The cyclic buckling tests were performed on the nanocomposite coatings at room temperature using an MTS Tytron 250 testing machine (MTS Systems Corp.). The films were bent and stretched with a range of ± 0.75 mm, at a frequency of 1 Hz, for a total of 600 cycles.

Recycling test

A bulk nanocomposite sample was prepared as described above. After drying, a portion of the sample was removed using a razor blade and prepared for TEM imaging. The remainder of the bulk sample was weighed and placed in a 20-ml glass vial. Chloroform was used to dissolve the dried sample; the volume of chloroform was selected to produce a 2.5-vol% solution. The bulk sample seemed to dissolve immediately and the solution was stirred overnight to ensure complete dissolution. The following day, another bulk sample was prepared as described above. TEM imaging confirmed that the recycled sample had the same lamellar structure as the original sample (Extended Data Fig. 8).

STEM tomography

Projection images for 3D electron tomography were collected using a FEI TitanX 60-300 microscope with a 10-mrad probe semi-convergence angle operated at 200 kV at the National Center for Electron Microscopy (NCEM) facility of the Molecular Foundry. A hummingbird heavy tomography holder was used to acquire a series of TEM images at tilt angles in the range $\pm 70^\circ$ at an angular interval of 1°. The tilt series were aligned and reconstructed using the eTomo software of the IMOD tomography package. Reconstruction was done using the weighted-back-5 projection method. 3D visualization was performed using Tomviz 1.3.1.

Data availability

All data needed to evaluate the conclusions in the paper are present in the paper and/or the supplementary materials. Source data are provided with this paper.

47. Heller, W. T. et al. The suite of small-angle neutron scattering instruments at Oak Ridge National Laboratory. *J. Appl. Crystallogr.* **51**, 242–248 (2018).
48. Heller, W. T. et al. dritsans: the data reduction toolkit for small-angle neutron scattering at Oak Ridge National Laboratory. *SoftwareX* **19**, 101101 (2022).
49. Wignall, G. D. & Bates, F. S. Absolute calibration of small-angle neutron scattering data. *J. Appl. Crystallogr.* **20**, 28–40 (1987).
50. Ilavsky, J. & Jemian, P. R. Irena: tool suite for modeling and analysis of small-angle scattering. *J. Appl. Crystallogr.* **42**, 347–353 (2009).
51. Veseli, S., Schwarz, N. & Schmitz, C. APS data management system. *J. Synchrotron Radiat.* **25**, 1574–1580 (2018).
52. Murphy, J. N., Harris, K. D. & Buriak, J. M. Automated defect and correlation length analysis of block copolymer thin film nanopatterns. *PLoS One* **10**, 1–32 (2015).
53. United States Environmental Protection Agency. Compendium method TO-11A. Determination of formaldehyde in ambient air using adsorbent cartridge followed by high performance liquid chromatography (HPLC) (1999).
54. ASTM International. ASTM E96-00. Standard test methods for water vapor transmission of materials (2017).
55. O'Brien, F. E. M. The control of humidity by saturated salt solutions. *J. Sci. Instrum.* **25**, 73 (1948).
56. Oliver, W. C. & Pharr, G. M. An improved technique for determining hardness and elastic modulus using load and displacement sensing indentation experiments. *J. Mater. Res.* **7**, 1564–1583 (1992).

Acknowledgements This work was funded by the U.S. Department of Energy, Office of Science, Office of Basic Energy Sciences, Materials Sciences and Engineering Division, under contract DE-AC02-05CH11231 (Organic–Inorganic Nanocomposites KC3104). E.V. was supported by the

Department of Defense through the National Defense Science and Engineering Graduate (NDSEG) Fellowship Program. J.J. was supported by a National Science Foundation Graduate Research Fellowship under grant no. DGE 1752814. H.D. and X.T. acknowledge support from the Laboratory Directed Research and Development (LDRD) programme under contract no. DE-AC02-05CH11231. Membrane fabrication for VOC and water-permeability testing was supported by the Defense Threat Reduction Agency under contract no. HDTRA1-22-1-0005. Part of this research used resources at the Spallation Neutron Source, a DOE Office of Science User Facility operated by the Oak Ridge National Laboratory, the Advanced Photon Source operated by the Argonne National Laboratory, under contract no. DE-AC02-06CH11357, the Advanced Light Source and the Molecular Foundry operated by the Lawrence Berkeley National Laboratory under contract no. DE-AC02-05CH11231. We thank A. Minor for providing access to the nanoindentation measurements. Q.Z. thanks R. Ziegler and D. P. Jensen Jr. for technical assistance.

Author contributions T.X. and E.V. conceived the idea and guided the project. E.V., L.M., K.M.E. and T.X. studied supramolecular phase behaviours. E.V. developed the fabrication process, analysed the growth process and prepared coatings for testing, with assistance from V.L.T. Q.Z. assisted with XPCS data collection and analysis. J.K. and R.O.R. performed mechanical-property

measurements. X.T. and H.D. performed VOC barrier testing. H.L. and Y.L. performed dielectric measurements and synthesized small molecules for control studies. W.-R.C. and W.H. performed the USANS studies and assisted with the data analysis. I.K. and J.I. helped collect the USAXS measurements. J.J. and A.C.A. performed electrical calcium conductivity tests of calcium protected by the nanocomposite and control barriers.

Competing interests T.X., E.V. and L.M. have a pending PCT patent application. The remaining authors declare no competing interests.

Additional information

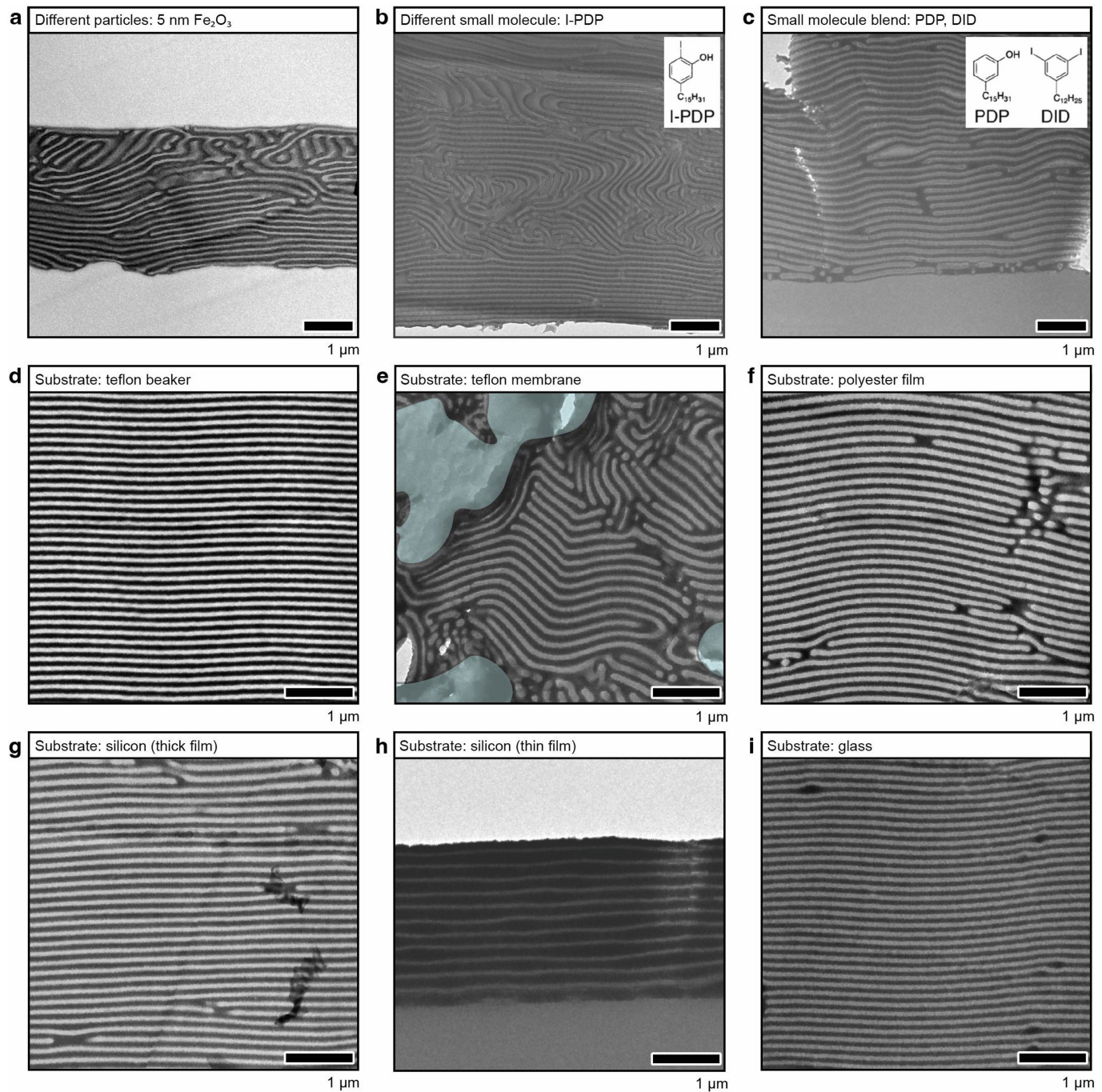
Supplementary information The online version contains supplementary material available at <https://doi.org/10.1038/s41586-023-06660-x>.

Correspondence and requests for materials should be addressed to Ting Xu.

Peer review information *Nature* thanks Darrin Pochan, Du Yeol Ryu and the other, anonymous, reviewer(s) for their contribution to the peer review of this work. Peer reviewer reports are available.

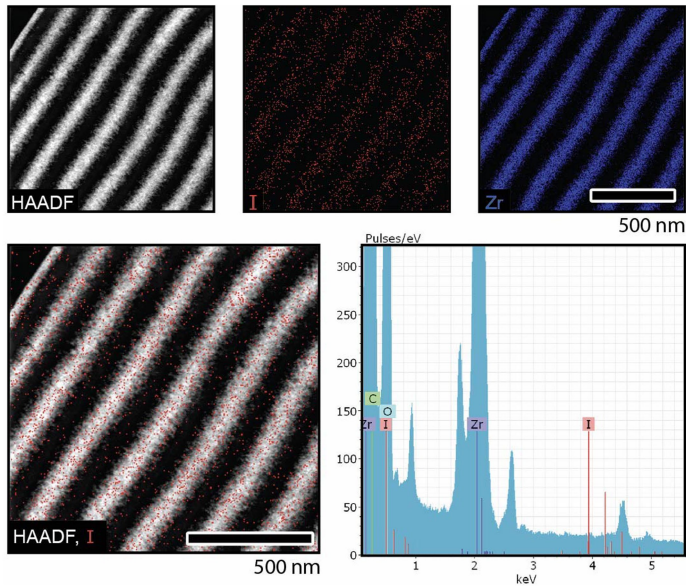
Reprints and permissions information is available at <http://www.nature.com/reprints>.

Article



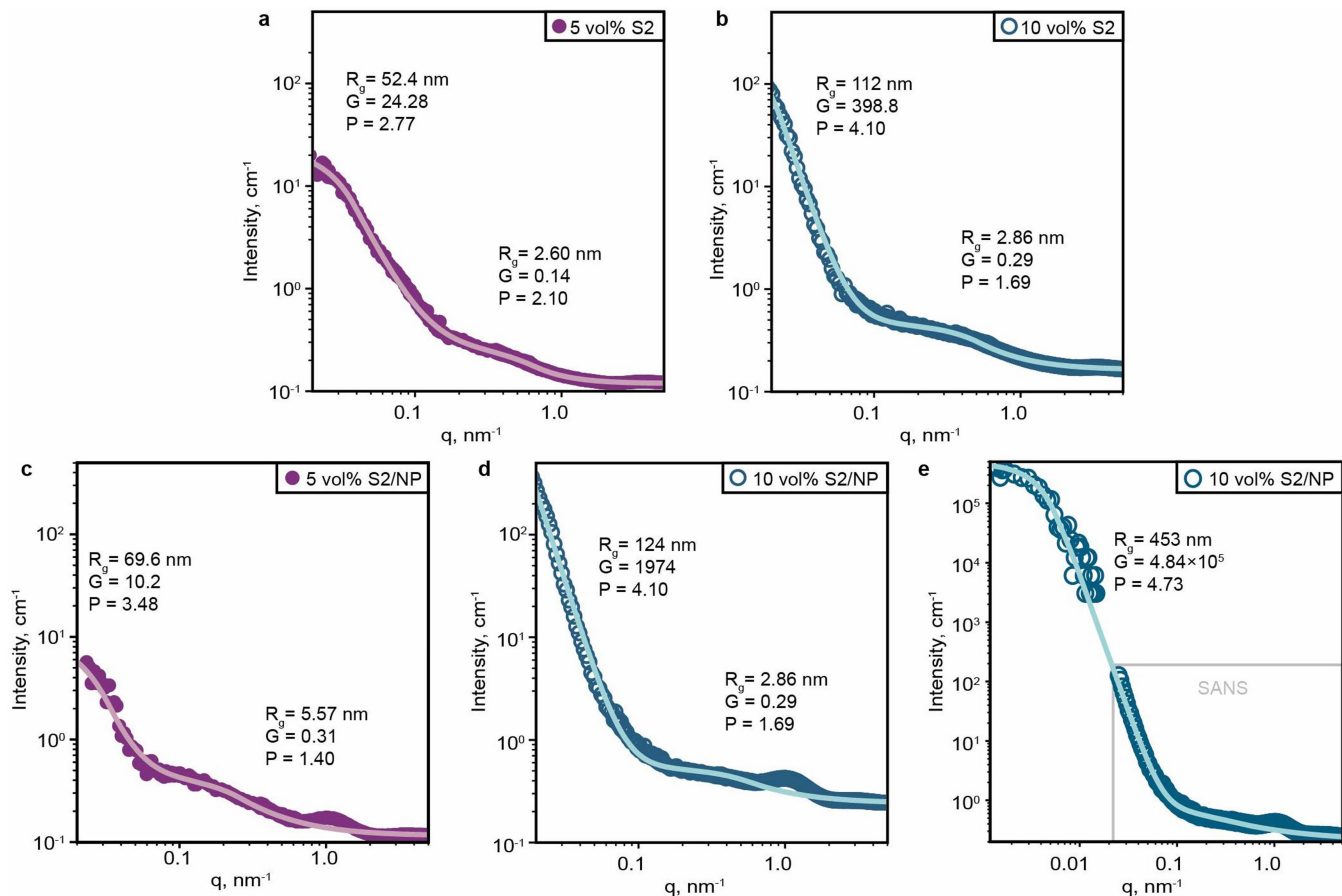
Extended Data Fig. 1 | Formulation flexibility and system versatility. TEM images of variations on the S2/NP blend formulation. **a**, S2 supramolecules with 6 vol% 5 nm iron oxide nanoparticles. **b**, 330-*b*-125 kDa supramolecules formed using a different hydrogen-bonding small molecule, I-PDP (inset). This is the same blend used for EDS analysis. **c**, 330-*b*-125 kDa supramolecules formed

using a blend of hydrogen-bonding (PDP) and non-hydrogen-bonding small molecules (DID) at molar ratios of 1 and 0.6, respectively. **d–i**, S2/NP blends self-assembled on a variety of substrates: a Teflon beaker, a porous Teflon membrane, a polyester film, a silicon wafer (thick and thin films shown) and glass.



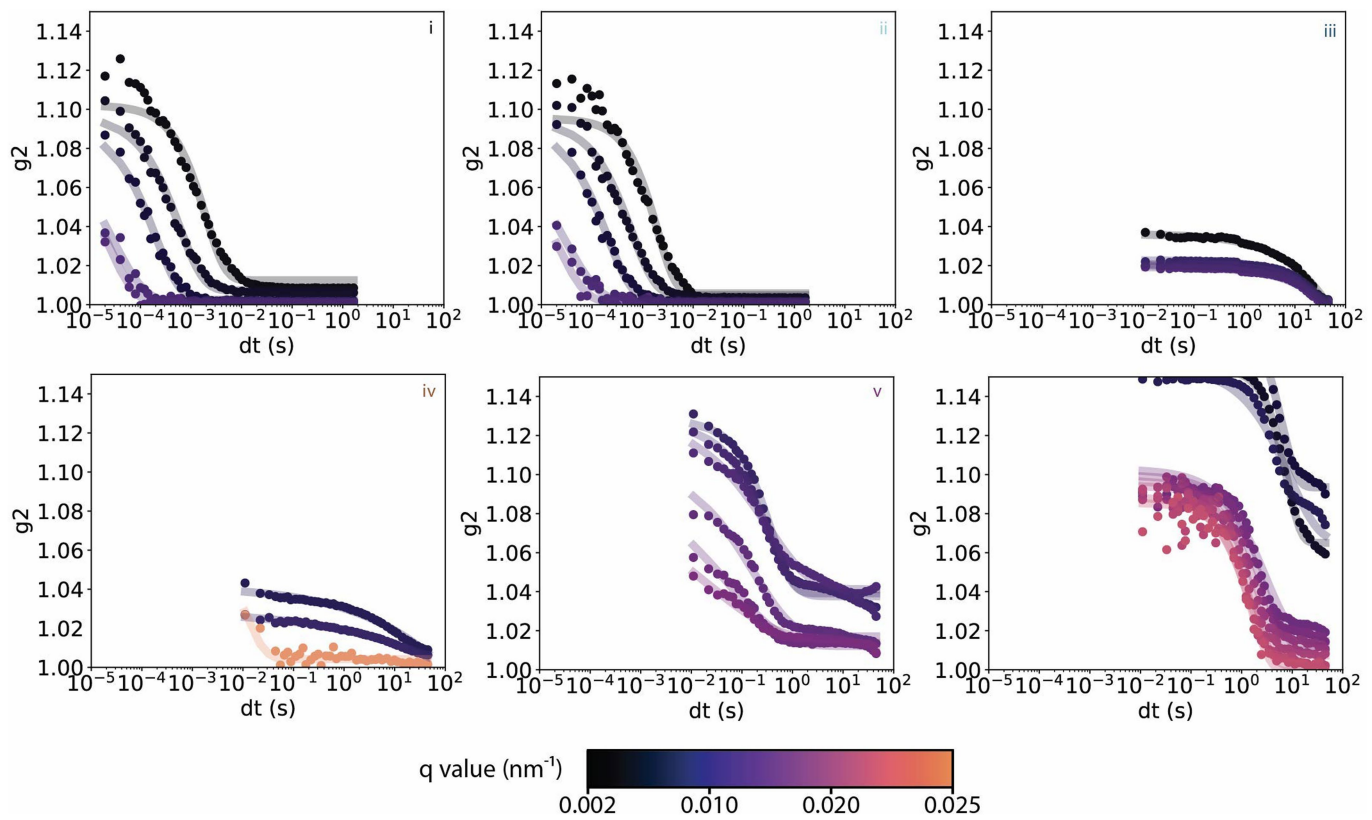
Extended Data Fig. 2 | EDS with I-PDP. Iodine-labelled small molecules are used to show the small-molecule distribution in a S2/NP blend. The structural and chemical information is collected using a high-angle annular dark-field set-up, so the contrast is reversed compared with the other TEM images shown in this work. The brightest pixels are those that scatter most strongly, so the nanoparticle-filled domains are lighter than the organic-only domains. The

iodine map shows that I-PDP are distributed throughout all microdomains, despite the enthalpic driving force for them to segregate into the P4VP(PDP) domains. By comparison, the ZrO_2 nanoparticles are strictly partitioned into the P4VP(PDP) domains. This imaging technique does not differentiate between hydrogen-bonded and unbonded small molecules, so the P4VP(PDP) domains have an overall higher concentration of small molecules.

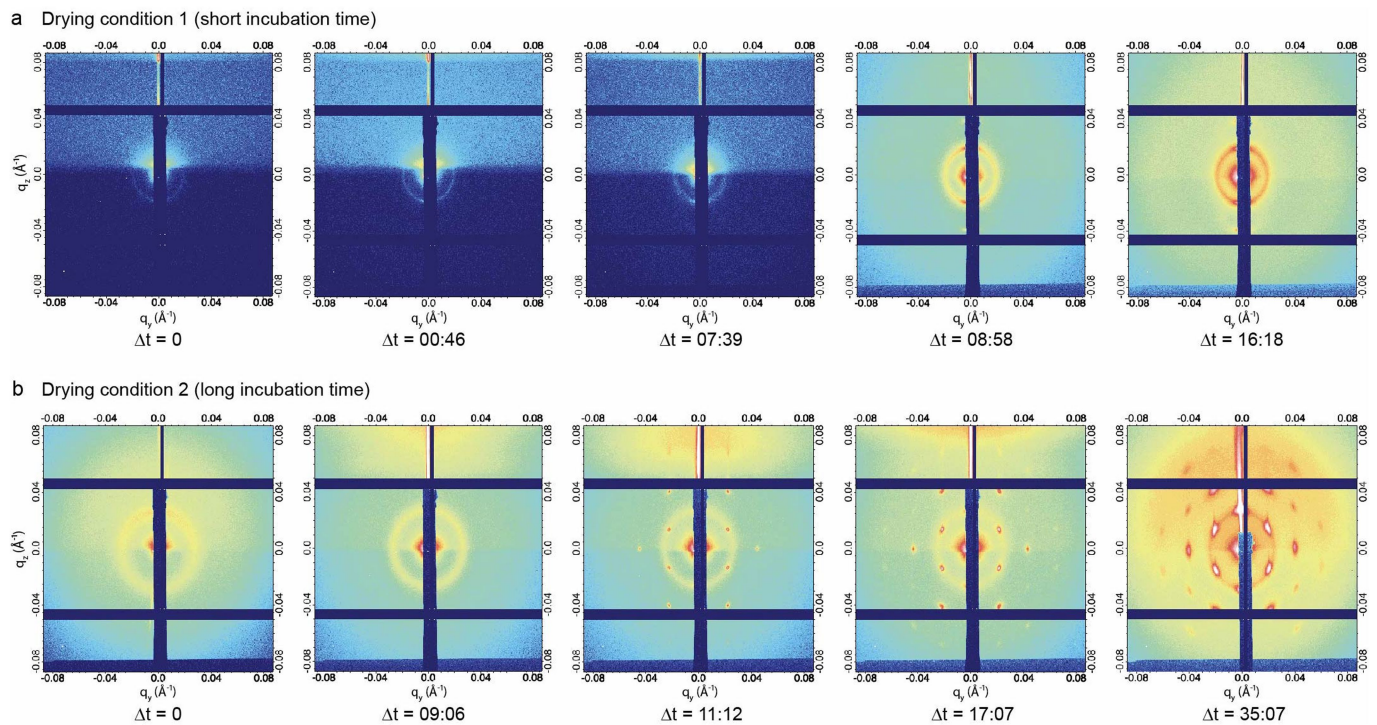


Extended Data Fig. 3 | Guinier-Porod fits of solution USANS data. **a–d**, Every SANS curve is fit with a two-part model, with the higher- q part representing the behaviour of individual supramolecules and the lower- q part representing the behaviour of the nanosheet aggregates. **e**, In the case of the USANS data, a third lower- q part is added to represent the collective behaviour of the nanosheets. Critically, the USANS data are absolutely calibrated, so the magnitude of the scattering intensity can be compared across samples. Compared with the solvent, the supramolecules have a lower scattering length density (SLD) and the nanoparticles have a higher SLD. The 5-vol% S2 solution has markedly higher scattering intensity than the 5-vol% S2/NP solution. This is consistent

with isolated nanoparticles distributed throughout the supramolecular aggregates. If the nanoparticles are distributed evenly throughout the supramolecular aggregates, the spatially averaged SLD will be more similar to the surrounding solvent and a lower overall intensity is expected. If the particles were instead packed densely in specific regions of the supramolecular aggregates, the SLD contrast would be greater than in the sample without particles and higher scattering intensity would be seen. Indeed, this is exactly the trend we observe in the 10-vol% S2 and S2/NP solutions. This analysis is discussed further in the Supporting Information.

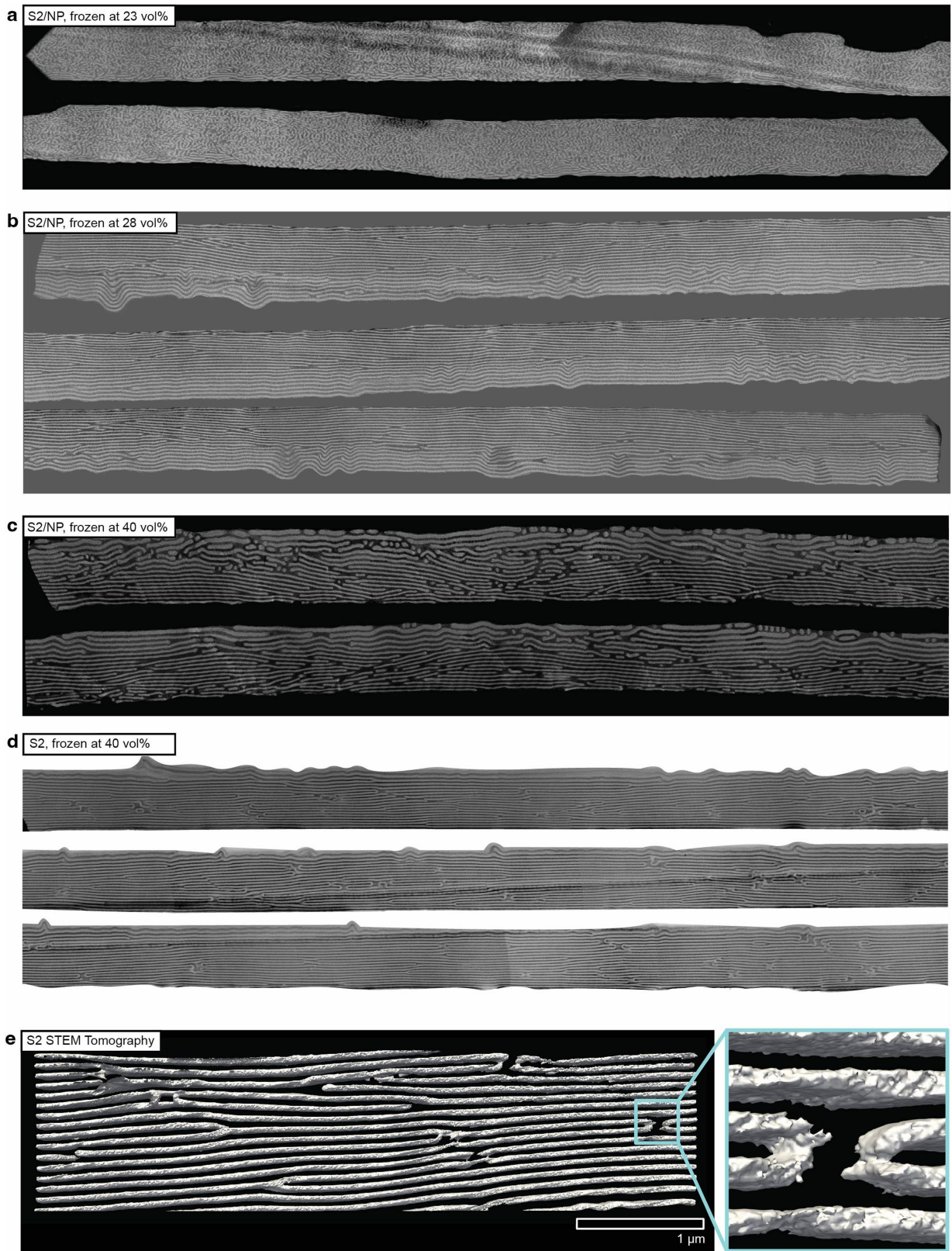


Extended Data Fig. 4 | Compiled g_2 plots for in situ XPCS. These panels show g_2 data corresponding to the assembly stages i–iv labelled in Fig. 2d–f. The first two g_2 plots used the ‘fast dynamics’ set-up and the remaining four use the ‘slow dynamics’ set-up.


Extended Data Fig. 5 | In situ GTSAXS of S1^{cyl}/NP for two drying conditions.

We varied the incubation time Δt between the formation of molecular aggregates, indicated by a diffuse scattering ring ($q = 0.027 \text{ \AA}^{-1}$, full width at half maximum = 0.0058 \AA^{-1}) and the formation of cylindrical microdomains ($q = 0.026 \text{ \AA}^{-1}$, full width at half maximum = 0.0013 \AA^{-1}). Δt is defined as $t_f - t_i$, in which t_i is the time elapsed between the initial solution deposition and the first appearance of molecular aggregates. For two different drying conditions, the

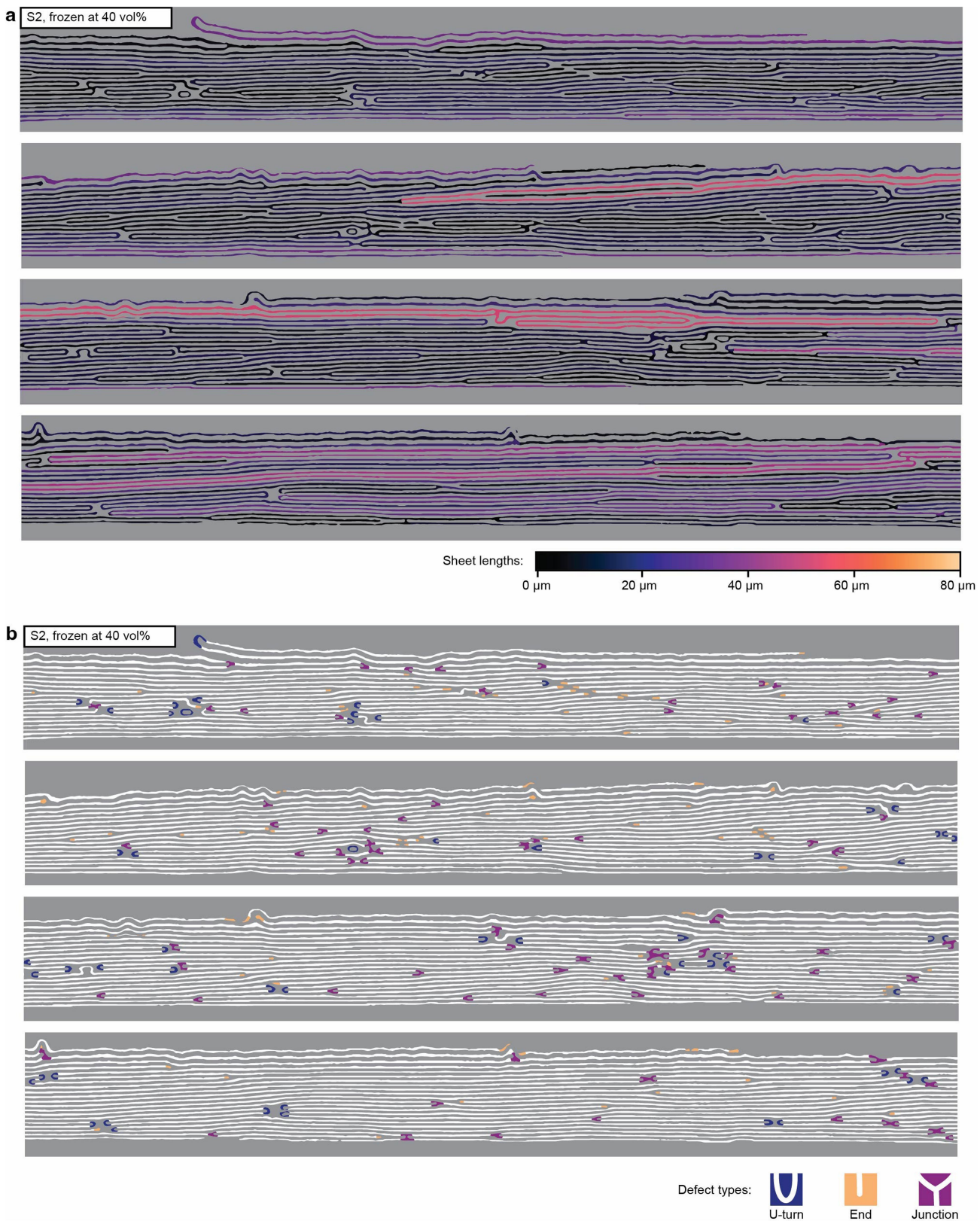
first appearance of molecular aggregates ($\Delta t = 0$) is shown on the left. For drying condition 1, $t_i = 23:28$ min; for drying condition 2, $t_i = 49:18$ min. As shown below, when $\Delta t < 1$ min, the final film is poorly ordered. When $\Delta t = 11$ min, the film forms highly ordered, hexagonally packed cylindrical microdomains, seen as sharp, highly ordered diffraction peaks. The results are consistent with the XPCS studies of S2/NP shown in the main text. Thus, long-range order can be obtained by varying Δt for morphologies other than lamellae.



Extended Data Fig. 6 | Large-area TEM images and STEM tomography. The TEM images were used to calculate defect densities and sheet lengths for thick and thin films. STEM tomography reconstruction was performed for a S2 film.

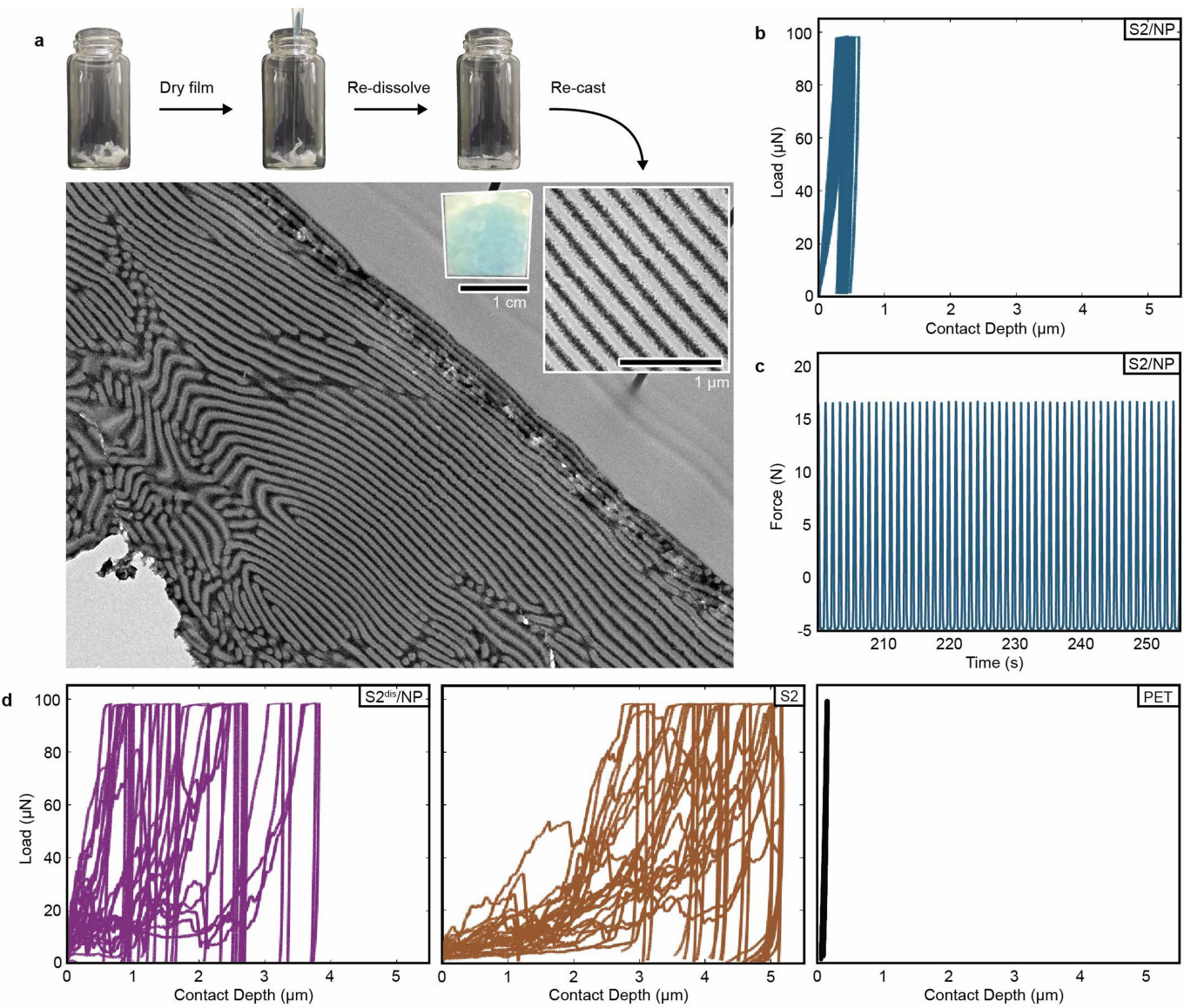
The U-turn defect reconstructions confirmed that these characteristic defects are indeed continuous nanosheets folded at a sharp angle.

Article



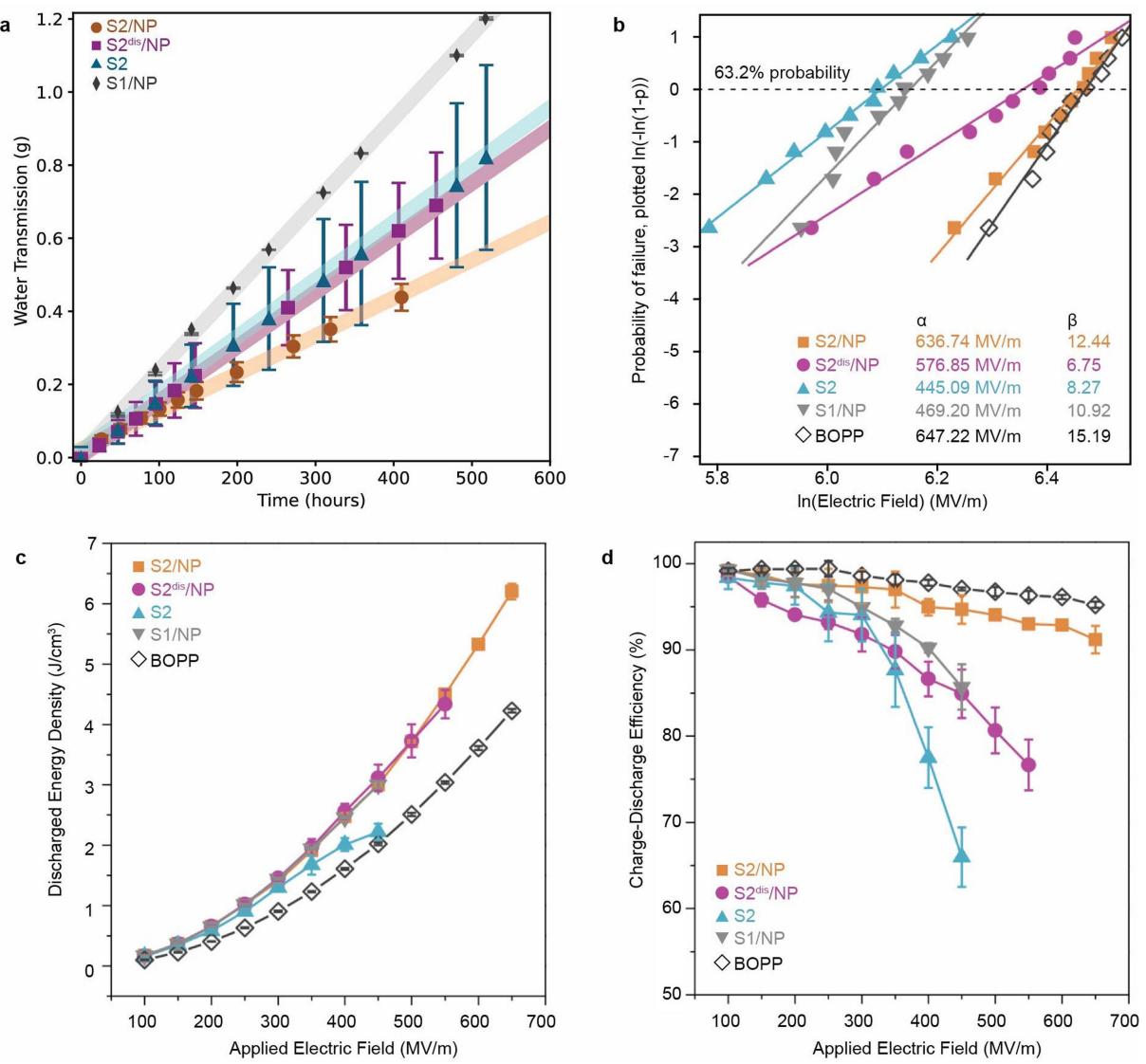
Extended Data Fig. 7 | Images and data for defect density and sheet-length analyses. Examples of an automated sheet-length analysis and a semi-automated defect-density analysis, performed on the S2 film frozen at 40 vol%.

As described in Methods, junction and ends were identified automatically. U-turn defects were labelled manually.



Extended Data Fig. 8 | Stability analysis: recycling, nanoindentation and cyclic bending. **a**, When a film is dried, redissolved and then recast, it forms the same lamellar structure as before. **b**, Nanoindentation results show that S2/NP films are mechanically stable despite the lack of chemical crosslinks between layers. **c**, Cyclic buckling tests ($n = 600$) of S2/NP on a PET film show

that the film remains intact without any delamination from the substrate. **d**, Disordered nanocomposites (S2^{dis}/NP) and lamellae without nanoparticles (S2) both had inferior properties, although all tested films had the same thickness and were supported by the same PET film.



Extended Data Fig. 9 | WVTR and dielectric barrier test results. **a**, The WVTR values reported in the main text come from the linear fits on the time series data shown below. **b**, The dielectric results include Weibull plots of dielectric breakdown strength for S2/NP, S2^{dis}/NP, S2 and S1/NP films. Discharged energy

density (**c**) and charge–discharge efficiency as a function of applied electric field (**d**) of S2/NP, S2^{dis}/NP, S2 and S1/NP films. Dielectric performance for commercial BOPP is also plotted as a control sample.